2012

Photoexcitation and Exciton Transport in Molecular Crystals

Pavel Irkhin
Lehigh University

Follow this and additional works at: http://preserve.lehigh.edu/etd

Recommended Citation

Irkhin, Pavel, "Photoexcitation and Exciton Transport in Molecular Crystals" (2012). *Theses and Dissertations.* Paper 1049.

Photoexcitation and Exciton Transport
in Molecular Crystals

by

Pavel Irkhin

A Dissertation
Presented to the Graduate Committee
of Lehigh University
in Candidacy for the Degree of
Doctor of Philosophy
in
Physics

Lehigh University
September 2012

Approved and recommended for acceptance as a dissertation in partial fulfillment of the requirements for the degree of Doctor of Philosophy.

Pavel Irkhin
Photoexcitation and exciton transport in molecular crystals

_____
Date

_____
Ivan Biaggio, Dissertation Director, Chair

_____
Accepted Date

Committee Members

_____
Volkmar Dierolf

_____
Slava V. Rotkin

_____
Nelson Tansu

iii

Acknowledgements

First of all, I would like to thank my advisor, Professor Ivan Biaggio, who created a positive and comfortable atmosphere for my work, and for all the various things I have learnt from him (which is a lot).

Second, I have to thank my committee members, Professors Volkmar Dierolf, Slava V. Rotkin, and Nelson Tansu, for all their ideas, interesting discussions, and help throughout the process. I owe special thanks to Professor Rotkin for his strong interest in my work, and his contribution to the quality of this dissertation.

And, of course, I thank our collaborators, my research group, teachers and friends, machinists and secretaries of the Physics Department, for making these few years a productive and interesting experience for me.

Contents

List of Figures

Abstract

This work is dedicated to the investigation of exciton transport processes in organic molecular crystals, and to the optical characterization of an important organic semiconductor, rubrene single crystal. Rubrene is a high quality molecular crystal that has been found to have exceptional functionalities in electronic applications such as field effect transistors.

I present the intrinsic absorption and photoluminescence spectra of rubrene single crystals, deriving them from a series of experiments performed in different experimental geometries. I describe the absorption spectra for all three principal light polarizations in the crystal, and discuss how the strongly anisotropic absorption and emission properties affect the spectral characteristics of observed photoluminescence spectra. I identify vibronic progressions both in absorption and emission and discuss their parameters and the main vibrational modes that are responsible for them. Through careful analysis of the data, I arrive at a conclusion that absorption and emission of rubrene that is not polarized along a specific crystallographic and molecular direction (c-axis of the crystal, corresponding to the M-axis of the molecule) is not due to an electronic dipole matrix element that has components in that direction. Instead, it is caused by vibronically-induced depolarization of the

1

electronic HOMO-LUMO transition that is described by a dipole matrix element that has components along the c-axis.

Further, this work developed and demonstrated a direct imaging technique that allowed to directly observe the diffusion of excitons in rubrene single crystals. This simple and intuitive technique uses localized photoexcitation and spatially resolved detection of the excitonic luminescence to visualize the spatial distribution of excitons. The technique was then used to directly measure the diffusion length of triplet excitons in rubrene. To do this, I exploited the fact that in rubrene photoexcited singlet excitons undergo efficient fission into triplet excitons, and the latter can interact with each other to create photoluminescing singlet excitons again.

I show that the exciton mobility in rubrene is strongly anisotropic, with long-range diffusion by several micrometers associated only with the direction of molecular stacking in the crystal, the same direction for which a large charge carrier mobility has been observed in experiments with field effect transistors.

Chapter 1

Introduction

The physics of organic solids is on a borderline between a number of related disciplines—molecular physics, solid-state physics and electronics, organic and physical chemistry, and even molecular biology [1], and organic solids form a link between the physics of inorganic materials and biophysics. Today, the knowledge gained in this field provides the material and conceptual framework for the development of a new interdisciplinary branch of science and technology known as molecular electronics.

Molecular crystals formed by organic molecules poses mechanical, optical and electronic properties that strongly differ from that of conventional covalent or ionic crystals. The hierarchy of forces observed in this class of materials is responsible for many of the characteristic properties of organic solids: while covalent intramolecular bonds are strong, weak intermolecular forces give rise to the marked tendency of charge carrier and exciton localization, low mobilities and large effective masses [1–3]. This is mainly caused by the weak nature of the intermolecular Van der Waals type interaction forces.

More generally, one can define molecular crystals as a kind of solids formed by electrically neutral molecules held together by relatively weak, nonbonding interaction forces. In addition to the Van der Waals forces, some molecules that have specific functional groups can form intermolecular hydrogen bonds. Another example is a so-called charge transfer complex, where molecules interact via a partial electron transfer from the donor to the acceptor molecule [1].

An example of the simplest molecular crystal is the one formed by neutral noble-gas atoms, such as helium, krypton or xenon. Crystals formed by molecules of nitrogen or oxygen can be stable only at cryogenic temperatures due to a very weak interaction forces.

A famous example of a more stable molecular crystal, where polar molecules are held together by a network of hydrogen bonds, is an ordinary ice.

Most properties of organic molecular crystals in many cases can be understood by treating it like an "oriented molecular gas". This is mainly due to the fact that weak interaction forces produce only a slight change in the electronic structure of the individual molecules. On a formation of a solid phase, molecules in the lattice mostly retain their identity, in contrast with traditional covalent or ionic crystals characterized by a complete loss of properties of constituent particles in the crystal. As a result, the optical spectra of an isolated molecule and of a molecular crystal are often similar, and certain spectral features, including electronic-vibronic structure, remain unchanged. However, collective molecular interactions result in an emergence of certain new features, that are of a particular interest.

Intermolecular dynamics of charge carriers strongly governs the charge transport properties in molecular semiconductors, meaning that the degree of molecular order

is absolutely crucial for electrical conductivity, which makes organic semiconductor single crystals the best candidate.

This work focuses on optical and exciton transport properties of an important organic semiconductor, rubrene single crystal. In chapter 2, I discuss the main properties of a rubrene molecule, and of a rubrene crystal. Chapters 3 and 4 present a detailed study of the optical absorption and photoluminescence properties of rubrene. In chapter 5, I discuss various experimental pitfalls and artifacts that have led to a large variability in the data, its interpretations and misinterpretations, in the existing literature. Then, I present a theoretical model that was used to rationalize the intrinsic spectroscopy data. In chapter 6, I describe a technique that I developed and demonstrated, that allowed to directly observe diffusion of excitons in rubrene single crystals. Finally, chapter 7 touches on some additional experiments I have performed with rubrene, gives global conclusions, and outlook.

Chapter 2

Rubrene molecule and rubrene single crystal

2.1 Introduction

The optical absorption and photoluminescence (PL) spectra of organic molecular crystals depend on the optical properties of the constituent molecules, on the geometrical arrangement of the molecules in the crystal matrix, and on intermolecular interactions. The rubrene single crystal has a large optical anisotropy that has a strong influence on the absorption and luminescence spectra that are observed under different experimental conditions. Although transport properties of rubrene single crystals have been extensively studied, considerably fewer studies have explored their optical properties, in particular the characteristics of the observed photoluminescence.

Among several organic materials that have been used as organic semiconductors,

e.g. in organic field effect transistors [4–6], photovoltaic cells [7], or light emitting diodes [8], rubrene single crystals are of particular interest because of several compelling properties, including one of the highest room-temperature charge carrier mobilities ever observed in an organic material ($\sim$ 10-40 cm^{2}V^{-1}s^{-1} for holes in field-effect transistors [4, 9–12]) and a high photoconductivity [13–15]. The high hole mobility values in rubrene crystals are found along the crystallographic direction characterized by a herringbone packing with an efficient π-overlap.

The properties of the rubrene molecule and how it is oriented in the crystal introduce a peculiar sensitivity of the detected photoluminescence spectrum from the experimental conditions, such as which facet of a crystal is illuminated, surface quality of a crystal facet, and the wavelength used for photoexcitation. Because of this, photoluminescence spectra of rubrene single crystals reported up to now (See, e.g., Refs. [16–25]) partially contradict each other both in the actual data as well as in the interpretations proposed by the various authors.

In the following, I present a detailed review of the way in which different experimental conditions give rise to large variations in the detected photoluminescence spectra. I then extract the intrinsic emission spectra taking into account the anisotropic absorption of orthorhombic rubrene and the excitation/detection conditions, identifying the underlying emission bands and their energies.

2.2   Rubrene molecule

In general, absorption and photoluminescence spectra of organic crystals have a molecular exciton signature that is strongly influenced by the optical properties
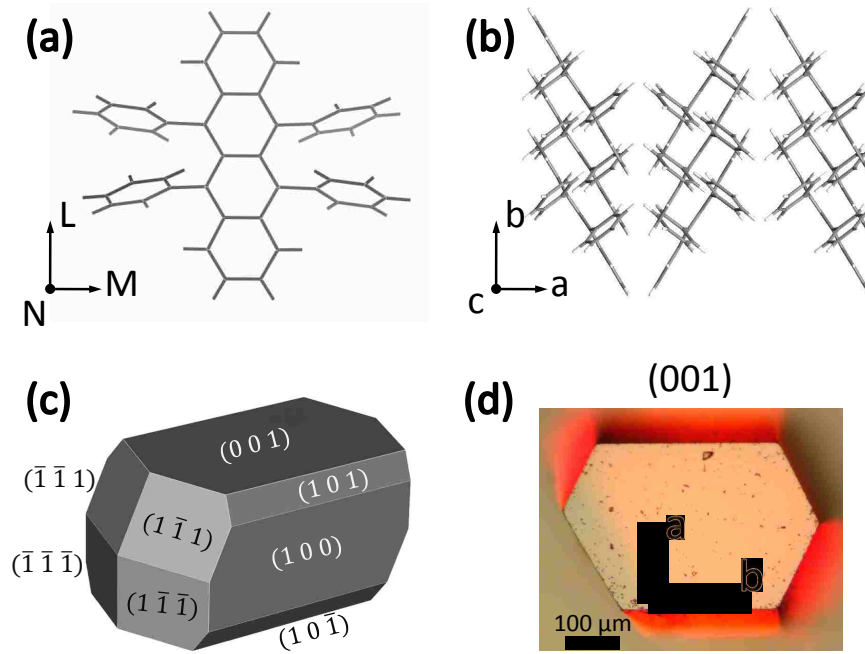
Figure 2.1: (a): rubrene molecule; (b): rubrene crystal structure in the *ab* plane; (c): simulated [26] habit of a rubrene single crystal; (d): image of a micrometer-sized stubby rubrene single crystal.

of the individual molecules. Below, I first review optical excitation and emission properties of a rubrene molecule.

Rubrene (5,6,11,12 - tetraphenylnaphthacene) belongs to the group of polycyclic aromatic hydrocarbons and is known as a sensitiser in chemoluminescence and as a yellow light source in lightsticks (Fig. 2.2, bottom). Rubrene molecule consists of four benzene rings (a molecular backbone structurally equal to tetracene) and four substituted phenyl groups attached to the two internal rings. The rubrene molecule as it is found in orthorhombic rubrene single crystals [27] is centrosymmetric, with a symmetry corresponding to the point group $2/m$, or C_{2h}, and a twofold axis of rotation (M-axis) along the short backbone. This molecular structure and the
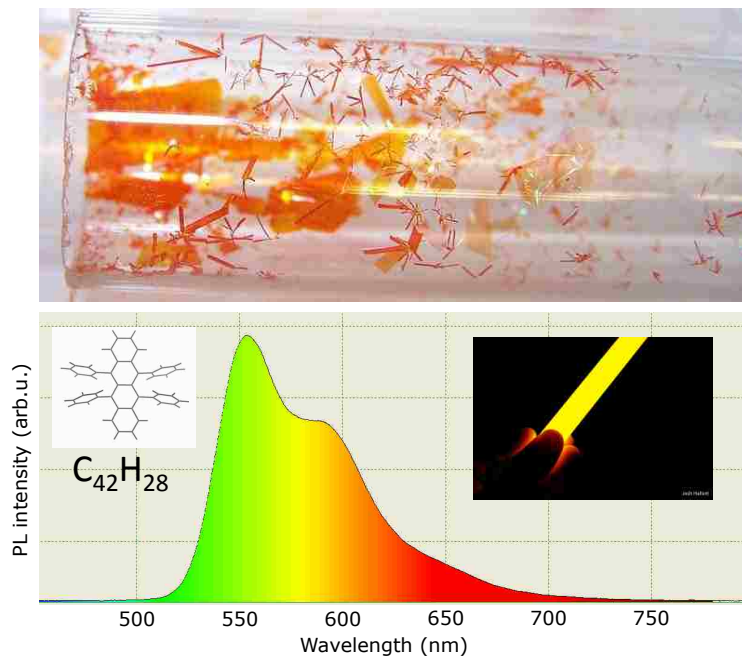
Figure 2.2: Top: rubrene single crystals growth by physical vapor transport method; Bottom: emission spectrum of rubrene in acetone; Inset: rubrene molecule (left), rubrene-based glow stick (right).

direction of the L, N, and M axes are shown in Fig. 2.1a. It should be noted that this structure differs in chirality as well as in the angles between the tetracene backbone and the phenyl side groups from the minimum-energy configuration of the rubrene molecule as can be obtained in quantum-chemical calculations [28, 29].

The molecular symmetry C_{2h} allows one to categorize the symmetry of all its states by the four irreducible representations A_g, A_u, B_g, B_u, where A/B refer to states symmetric/antisymmetric with respect to the rotation by 180° (C_2), while the subscripts u/g refer to odd/even parity with respect to the inversion operation. The Highest Occupied Molecular Orbital (HOMO) and the ground state of the molecule belong to the totally symmetric representation A_g. A dipole allowed transition can
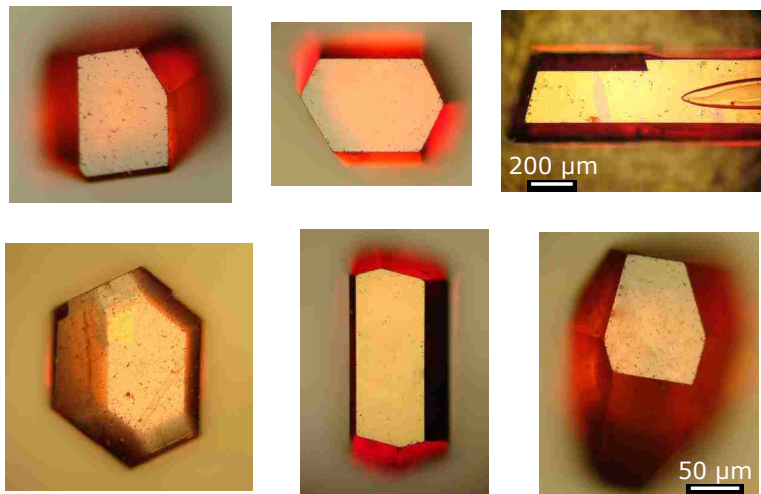
Figure 2.3: Images of various facets of rubrene single crystals.

occur to excited states that belong to either the A_u or B_u representations. The A_u state corresponds to the Lowest Unoccupied Molecular Orbital (LUMO), while the B_u state is the next higher state. The (L, N, M) components of the dipole operator in the C_{2h} point group have symmetries (B_u, B_u, A_u). HOMO-LUMO transitions $(A_g \leftrightarrow A_u)$ are only dipole allowed for a dipole operator of symmetry A_u, because $A_g \otimes A_u \otimes A_u = A_g$. They therefore occur for light polarized along the M axis of the molecule (Fig. 2.1a). On the other hand, transitions to and from the higher B_u state require a dipole operator with symmetry B_u (because $A_g \otimes B_u \otimes B_u = A_g$), and are therefore associated with light polarized along the L or N axes of the molecule. Transitions between the excited states (symmetry A_u and B_u) are not dipole allowed in this centrosymmetric molecule. A more detailed group theory discussion is given in section 5.2.

2.3 Rubrene single crystal

Vapor transport [30] grown rubrene crystals (Fig. 2.2, top) are orthorhombic [27], with D_{2h}^{18} (or mmm) point group and four molecules per unit cell. In this work, I define the crystallographic axes in the space group $Acam$, in which the lattice constants are $a = 14.4$ Å, $b = 7.18$ Å, and $c = 26.9$ Å instead of $Cmca$, as used in Ref. [27], where a (instead of c) corresponds to the long axis. The reason for this choice is that it is consistent with the labeling of the axes used in several charge transport experiments [10, 13].

Fig. 2.1b shows the molecular stacking along the mirror plane of the crystal (ab-plane). The L and N axes of the molecules are parallel to the ab plane of the crystal, while the M axes are all parallel to the c direction. When viewed along the normal to the surface, the boundaries of the growth facets parallel to the $\{001\}$ planes form an angle of 63.5 degrees to the b-axis, while the boundaries or growth facets parallel to the $\{100\}$ planes form an angle of 75 degrees to the b-axis [31] (Fig. 2.1c).

The most common shapes among as-grown rubrene crystals are platelets with extended c-surfaces and crystals elongated in the b-direction but with small thickness along the c-direction (Fig. 2.2, top). Crystal growth also delivers some high-quality stubby crystals with more equilibrated dimensions (up to ~ 500 μm) in the three spatial directions (Fig. 2.3). Such crystals exhibit various $\{ijk\}$ surfaces with indices between 0 and 2. The analysis of the crystal habit reveals characteristic geometries for the confining surfaces, which offer an unambiguous identification of the orientation of each surface. The larger of such crystals sometimes form $\{112\}$ surfaces. I observed that the photoluminescence properties of such crystals are very stable and do not change even over several years.

Chapter 3

Optical absorption of the rubrene single crystal

3.1 Polarized absorption spectra of the rubrene single crystal

The dipole matrix element for the lowest energy electronic transition from the ground state of the rubrene molecule has only one component, corresponding to the molecular M-direction. This property, coupled with the fact that all molecules in orthorhombic rubrene have their M-axes parallel to each other, creates a very large absorption and emission anisotropy in rubrene. The strong anisotropic absorption has an extremely large influence on the observed photoluminescence spectra that can be obtained from rubrene single crystals under different illumination and detection geometries. Before presenting the PL results in the next section, it is therefore necessary to first review and accurately determine the absorption spectra of rubrene

for light polarized parallel to the three crystallographic axes.

Since the strongest low-energy transition in the rubrene molecule is M-polarized, and since the M-axis of all molecules in rubrene is parallel to the c-axis of the crystal, I first discuss the absorption spectrum for light polarized along the c-axis. As-grown crystalline thin films and platelets have large surfaces that are normal to the c-axis. In order to determine the c-polarized absorption spectrum, I measured the transmission of rubrene crystalline thin films at oblique incidence for light polarized in the plane of incidence (Figure 3.1). Small, thin single crystals were observed under the microscope to make sure that all surfaces were unblemished. Both direct microscopic observation with a spatial resolution of 0.4 μm and interferometry were used to determine the thickness of the crystals, obtaining values between 0.8 μm and 5.0 μm for the samples used. Polarized white light was then focused onto the crystal with a 10$\times$ objective (Rayleigh range was always much larger than sample thickness), and the change in its spectrum after passing the crystal was measured with an Ocean Optics USB4000 fiber-coupled spectrometer by capturing the light with a second objective and focusing it into a multi-mode fiber of 100 μm diameter. I obtained calibrated absolute values for the sample transmission at each wavelength by measuring and correcting any polarization dependence in the reflectivity and transmission of the optical components used in the experiment. Several transmission spectra were collected starting at normal incidence and then for different rotations of the crystal around its a-axis(Figure 3.1). Angle-dependent reflection losses were calculated (Figure 3.2) from the refractive index values in the spectral range of interest ($n_a \approx 1.7, n_b \approx 1.9$, and $n_c \approx 2.0$ [31, 32]). I used interferometry to confirm the refractive index values and to confirm that index dispersion did not affect the
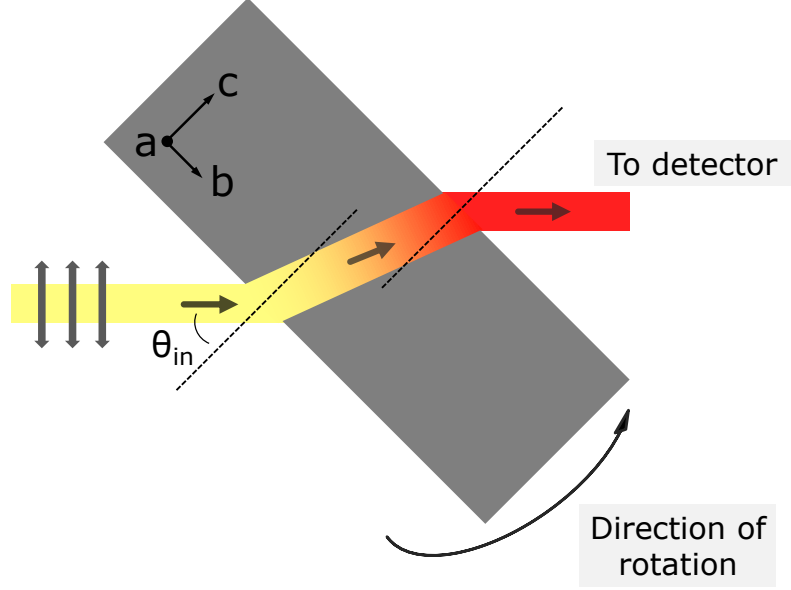
Figure 3.1: Experimental configuration for the absorbance measurements.

evaluation of the absorption spectra. Figure 3.3a shows absorbance spectra of a 2.7 μm thick rubrene crystal at normal and oblique angles of incidence. At moderate deviations from normal incidence, one immediately observes the emergence of a strong absorption band peaking near 2.32 eV (Fig. 3.3a).

The absorption constant for light polarized in the plane of incidence as a function of the angle θ between the surface normal and the wavevector of the light inside the crystal is

$$\alpha(\theta) = \alpha_{a,b}cos^2\theta + \alpha_c sin^2\theta \tag{3.1}$$

where α_a, α_b, α_c are the absorption constants for light polarized along the three
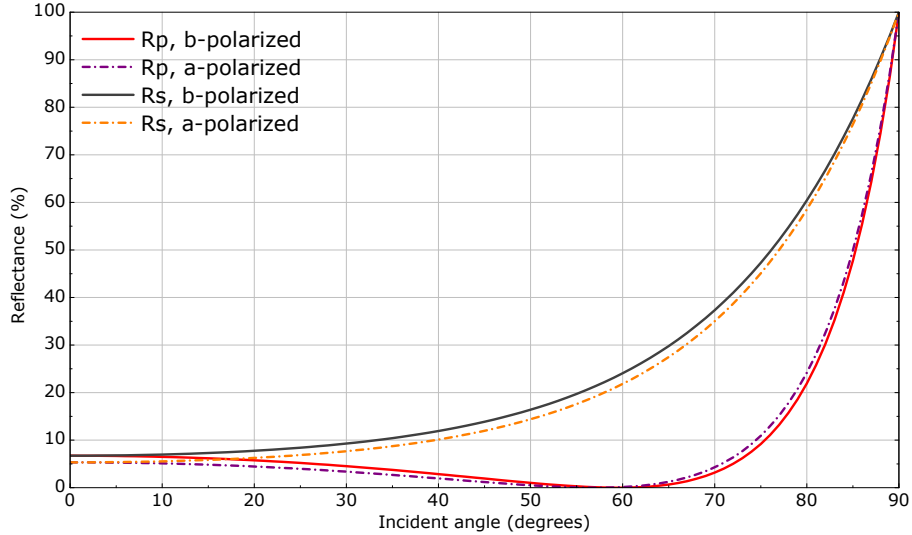
Figure 3.2: Reflectance of rubrene crystal surface for s- and p-polarized incident light. Angle dependence was calculated using Fresnel equations and refractive index values for a- and b-polarized light at 600 nm.

crystallographic axes, and in the above equation one must use either α_a or α_b depending on the experimental geometry. By calculating θ from the external angle using Snell's law and comparing the normal incidence spectra for α_a and α_b to the oblique incidence spectra for various values of θ between 10 and 50 degrees in several rubrene crystals, I extracted the full c-polarized absorption spectrum up to an energy of 3.0 eV. This spectrum is shown in Fig. 3.3b. The c-polarized absorption spectrum is dominated by a very strong band at 2.32 eV, followed by less intense bands at 2.49, 2.66, 2.83 and 3.00 eV, separated by 0.17 eV.

For comparison, Fig. 3.3c shows the absorption spectrum of rubrene dissolved in different solvents, and also of an amorphous molecular assembly of rubrene obtained by melting rubrene in an enclosure protected from atmospheric influences (e.g. oxidation). In all the spectra of Fig. 3.3c, the absorbance is caused by a rotationally
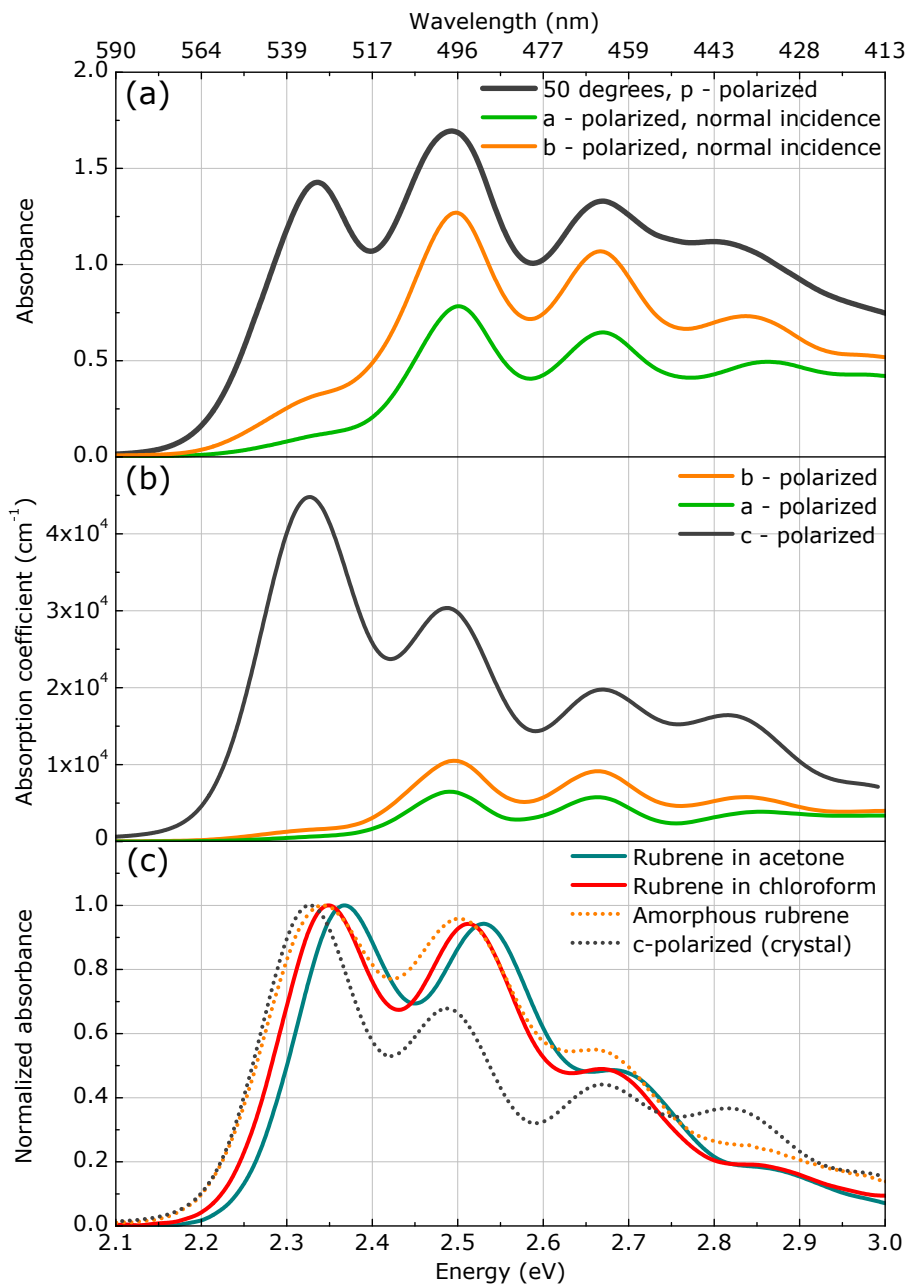
Figure 3.3: (a): Absorbance spectra of a thin (2.7 μm) rubrene crystalline film at normal and oblique angles of incidence on the ab plane; (b): absorption coefficients of rubrene for light polarized along the main crystal axes derived from multiple experiments; (c): normalized absorbance spectra of rubrene in solutions, amorphous solid, and normalized *c*-polarized absorbance of a rubrene single crystal.

averaged molecular orientation and is therefore dominated by the same transition dipole moment along the molecular M-axis that determines the c-polarized absorption spectrum in the crystal. The strongest absorption band for c-polarized light, observed at photon energy of 2.32 eV in the crystal, is clearly reflected in the spectra of Fig. 3.3c.

The absorption constant for light polarized along the a- and b-axes of the crystal was obtained from measurements taken at normal incidence. For a- or b-polarized light, the absorption spectra show a relatively strong band at 2.49 eV, followed by weaker bands at energy intervals of about 0.17 eV. The main features of these spectra agree with earlier reports in the literature [13, 17, 25]. The a- and b-polarized spectra also show a small shoulder near 2.32 eV, the energy of the strongest absorption peak visible in the c-polarized spectrum. This shoulder becomes more prominent whenever the light used to measure the absorption has a component that is c-polarized — as when the absorption is measured through more tightly focused beams, or when the incidence angle is not perfectly perpendicular to the ab-facet of the crystal, which causes a "leakage" of the strong c-polarized absorption. This raises the question if this band at 2.32 eV that is seen in a- or b-polarized spectra may be solely due to this leakage effect. It is certainly possible for a- or b-polarized measurement to overstate the size of this band. I have seen that the strength of this band can be minimized by measuring absorption using unfocused light, carefully aligning for normal incidence, and using crystals with higher surface quality. But can the whole band be an experimental artifact? From the fitting of the b-polarized absorption spectrum (Figure 3.4b, described in the next paragraph), I calculate an $\alpha_b = 400$ cm^{-1} at 2.32 eV that is exclusively due to the tail of the higher energy

bands, while the observed b-polarized absorption in the raw spectrum is 1.5×10^3 cm^{-1}. The value of α_c at the same photon energy is 4.5×10^4 cm^{-1}. From Eq. 3.1 one would need a deviation from normal incidence of the order of only 10 degrees (external angle) to obtain the observed (1500 cm^{-1}) b-polarized absorption band at 2.32 eV, assuming perfectly planar wavefronts ($\sim$ 5 degrees for a-polarized). Some misalignments, crystal imperfections, and/or light wavefront curvature could result in the observed band at 2.32 eV. The absorption spectra for a- and b-polarized light in Fig. 3.3b have been measured in a way that minimizes (but does not completely remove) the artificial enhancement of the absorption band at 2.32 eV that is caused by this leakage effect. From these observations, combined with additional insights obtained from the PL spectra analysis that will be presented below, I conclude that the observed shoulder at 2.32 eV is probably mainly caused by leakage of the c-polarized absorption, and should therefore not be considered as part of the intrinsic a- or b-polarized absorption spectrum of rubrene.

3.2   Analysis of the absorption spectra

To evaluate the position, amplitude, and width of the absorption bands contributing to the rubrene absorption spectra, I used a model spectrum consisting of a sum of separate bands to fit all absorption spectra between 2.1 and 3.6 eV. I made a special effort to minimize the number of fitting parameters by using the same identical Voigt profile for every spectral component and by using a sum of these Voigt profiles separated by a constant distance in energy. This corresponds to the simplest possible model for a set of equidistant vibrational levels that determine the
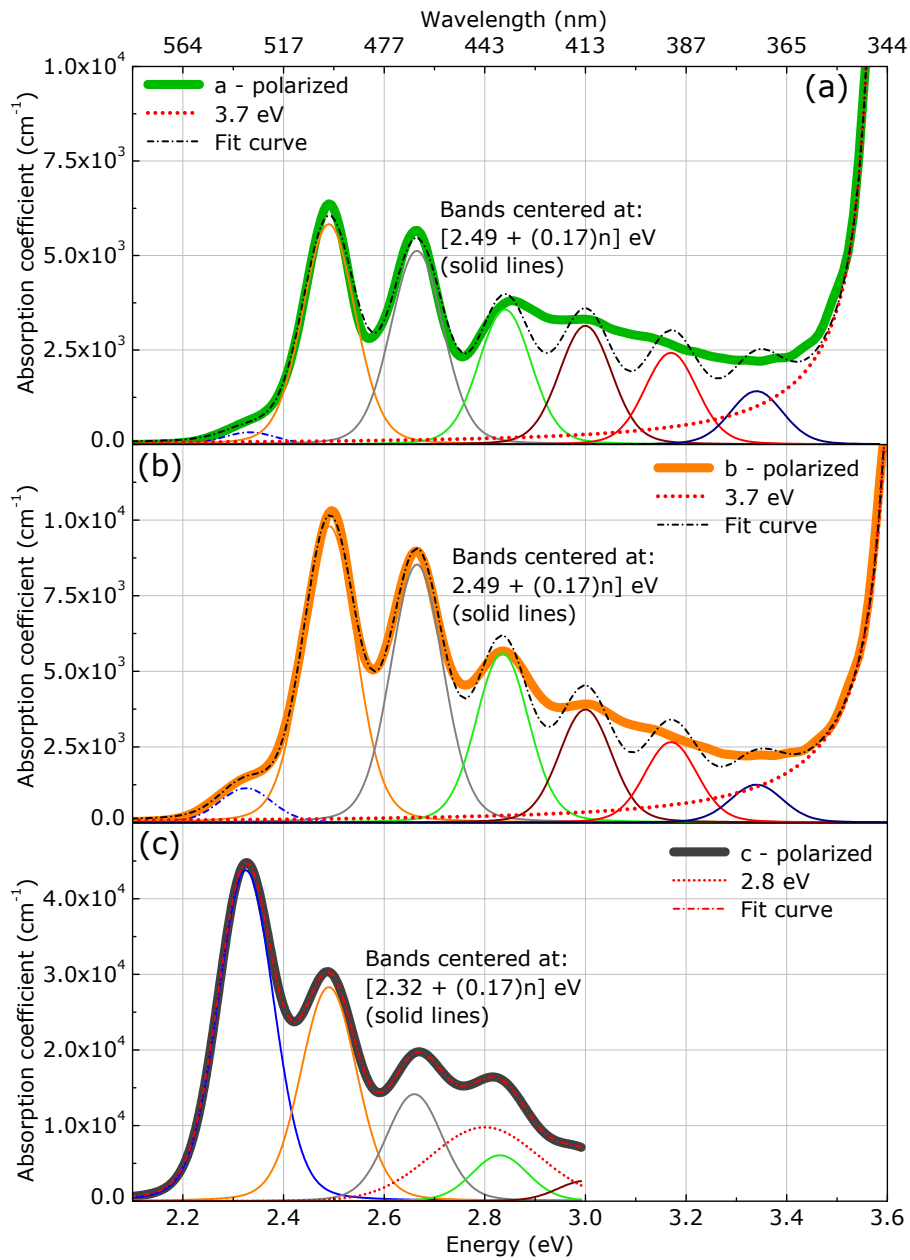
Figure 3.4: Peak fit of *a*-polarized (a), *b*-polarized (b) and *c*-polarized (c) absorption spectra.

vibronic progression. Thus, the only free parameters in the fit are the Lorentzian and Gaussian widths determining the shape of the Voigt profile used for all spectral components, the amplitude of each profile, the distance between them, and the position of the first absorption peak in the progression. In other words, curve-fitting of all 3 absorption spectra in Fig. 3.4 was done using 4 parameters for modeling the characteristics of the vibronic progression that all of them share, plus the amplitudes of the individual bands. In addition, to fit the ab polarized spectra I also considered the low-energy tail of the higher electronic state close to 3.7 eV [17, 32].

As can be seen in Fig. 3.4, the experimental absorption spectra can be closely reproduced using a sum of Voigt profiles with Full Width at Half Maximum (FWHM) of 0.12 eV and a ratio between Gaussian and Lorentzian widths of 5.6. The first band is at 2.32 eV, and it is followed by a sequence of higher energy bands, all separated by 0.17 eV. For the a- and b-polarized spectra (Fig. 3.4a-b), which extend to higher energy, the fitting function included the low-energy tail of the second electronic excited state. The absorption band at 2.32 eV that I have earlier assigned to an artificial "leakage" is drawn using a dash-dotted line. For the c-polarized spectrum (Figure 3.4c), the fitting function included an additional, noticeably wider band positioned at 2.8 eV. This band appears as a major difference between the absorption of a crystal and that of rubrene molecules in solution or in an amorphous solid, as can be seen in Fig. 3.3c. Such a band was also reported in the c-polarized absorption spectrum derived from ellipsometry data by Tavazzi et al. [33], where it was dominating the spectrum at around 2.8 eV, and the higher vibronic replicas were not resolved. I observed that the relative strength of this extra band slightly varies between samples of different thickness. The existence of this additional absorption

band at 2.8 eV is supported by a theoretical prediction of a quasiparticle band gap of 2.8 eV by Sai et al. [32]. Finally, I note that this simple model spectrum can reproduce the c-polarized spectrum extremely well, with the model function (dash-dotted line) practically indistinguishable from the data. On the other hand, there are deviations between fitted model function and data in the ab-polarized spectra between 2.8 and 3.4 eV that are clearly caused by the fact that I constrained the fitting function to a sum of equally separated vibrational bands with same shape and width. While it would be possible to obtain a better fit by also fitting position and width of the spectral components, such a fit would only increase the number of fitting parameters while not providing any additional information.

Chapter 4

Photoluminescence spectroscopy of the rubrene single crystal

4.1 Experimentally observed photoluminescence spectra

In this chapter, I review the different photoluminescence (PL) spectra that can be obtained from rubrene crystals under different experimental conditions. I excite the photoluminescence with a linearly polarized CW laser at 2.8 eV (442 nm) or 2.3 eV (532 nm). The laser beam is focused on the sample by a microscope objective, which also collects photoluminescence and images it onto an optical fiber coupled to a spectrometer (Figure 4.1). A linear polarizer is placed before the fiber to select the polarization of the detected PL. Longpass filters with appropriate edge wavelengths (488 nm for 442 nm excitation, 532 nm for 532 nm excitation, Figure 4.2) are used to remove the excitation light from the detected signal. All measurements were done
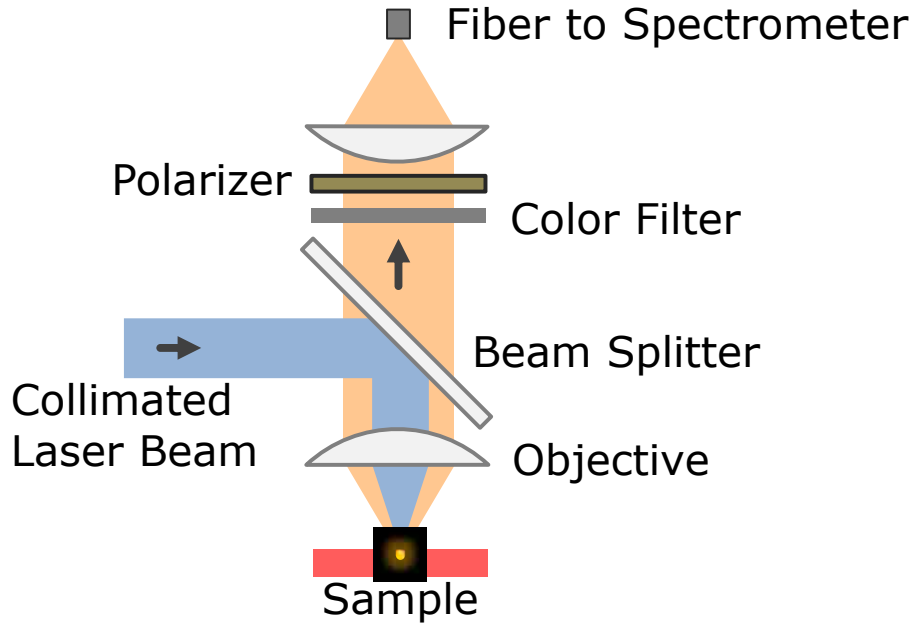
Figure 4.1: Experimental configuration for the photoluminescence measurements.

with an Olympus IX81 microscope to ensure a precise orientation of the crystal with respect to the direction and polarization of the excitation beam and for a precise control of crystal surface quality. As we will see later, this is very important for spectroscopy done on the *ab* facet, the largest as-grown surface of a rubrene crystal.

The raw PL spectra obtained from *ab* and *bc* facets of rubrene single crystals at two different excitation wavelengths are shown in Fig. 4.3. Each plot contains four curves, corresponding to the four possible combinations of excitation and PL polarizations. Each curve is labeled with a pair of letters to indicate the crystallographic axis along which the corresponding light polarization is oriented. The first letter gives the polarization of the excitation light; the second letter gives the
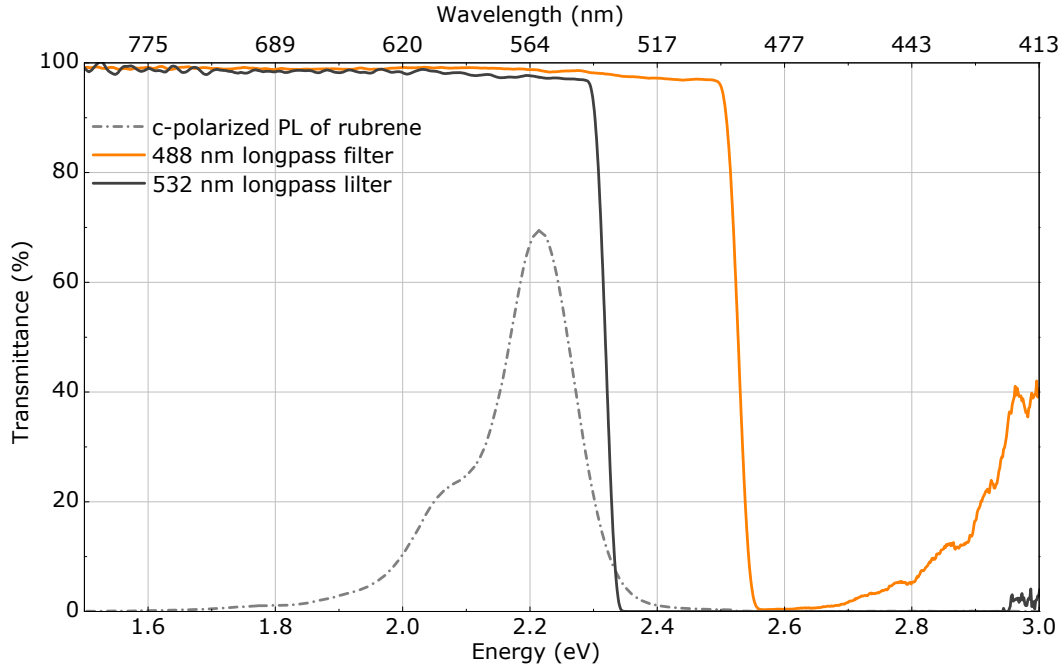
Figure 4.2: Transmission spectra on the longpass filters used, together with c-polarized PL spectrum of rubrene single crystals. I measured the transmittance spectra at normal incidence, the way it was actually used in the setup in Figure 4.1.

corresponding orientation of the analyzer in front of the PL detection system.

The vertical scale in the plots in Fig. 4.3 represents the same PL quantum efficiency for all excitation and emission polarizations belonging to the same excitation wavelength. One can therefore directly compare the strength of the PL when going from one experimental configuration to the other. To guarantee this I (1) kept the intensity distribution in the excitation spot and the laser power constant, (2) corrected all spectra for a polarization-dependent instrumental response (beam splitter transmittance (Figure 4.4), spectrometer sensitivity, etc.), and (3) made sure that the PL is collected with equal efficiency for all excitation/detection configurations by keeping the depth of field of the imaging system larger than the absorption length

24
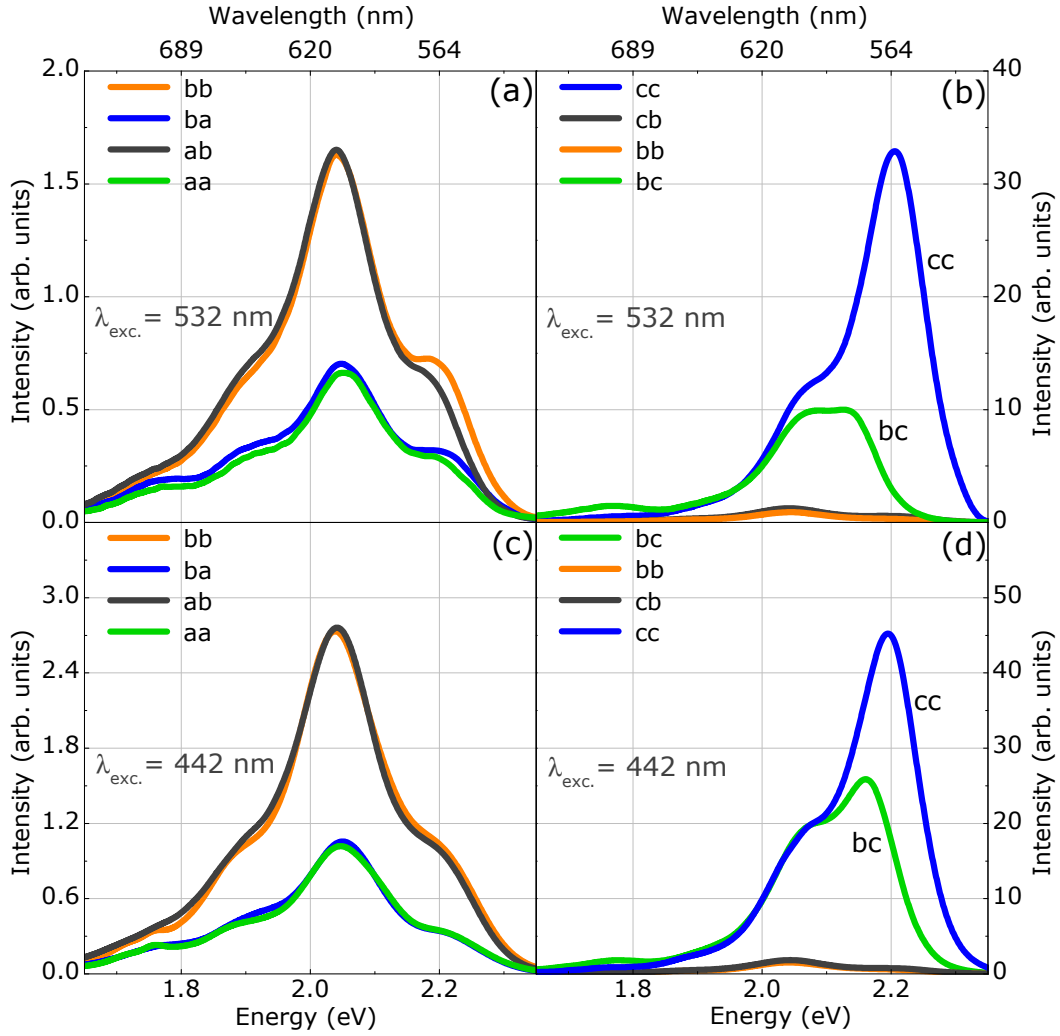
Figure 4.3: Top: photoluminescence spectra measured with 532 nm excitation on ab (a) and bc (b) facets. Bottom: photoluminescence spectra measured with 442 nm excitation on ab (c) and bc (d) facets. The vertical scale is in the same units for all spectra taken at the same excitation wavelength.

of the material at the excitation wavelength. At 442 nm, the absorption length of rubrene is about 3 μm for a-polarized light, 2 μm for b-polarization, and 0.6 μm for c-polarization (Figure 4.5). The corresponding values for 532 nm excitation are 15, 6 and 0.2 μm, respectively. I used a 10× objective with NA = 0.3 and a depth of
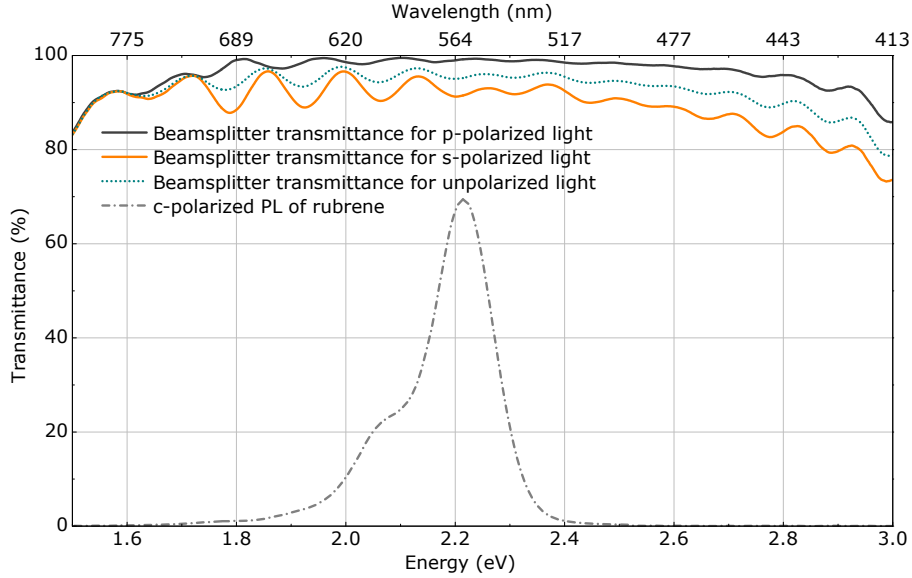
Figure 4.4: Polarization-dependent transmittance of beam splitters used, together with c-polarized PL emission spectrum of rubrene. I measured transmittance at 45 degree incidence, the way it was used in the setup in Figure 4.1.

field of 10 μm. In addition to having a large enough depth of field, using such an objective also guarantees that I capture the PL from all photoexcited excitons even in the presence of a 4 μm exciton diffusion length along the b-axis [34].

The raw spectra in Fig. 4.3 have several interesting features. First, I note that in the measurements in Fig. 4.3a,c the intensity of the PL emission does not depend on the *excitation* light polarization or wavelength, even though the absorption coefficients are different in all cases. The reason for this is that, in a thick crystal, the entire incident light is absorbed in a few micrometers independently of the polarization or wavelengths used, and the created PL is collected with the same efficiency. Then, I note that the b-polarized emission spectrum detected from the bc facet (Fig. 4.3b,d) is the same in amplitude and shape as the b-polarized emission spectrum detected from the ab facet, but it appears very small in Fig. 4.3b,d
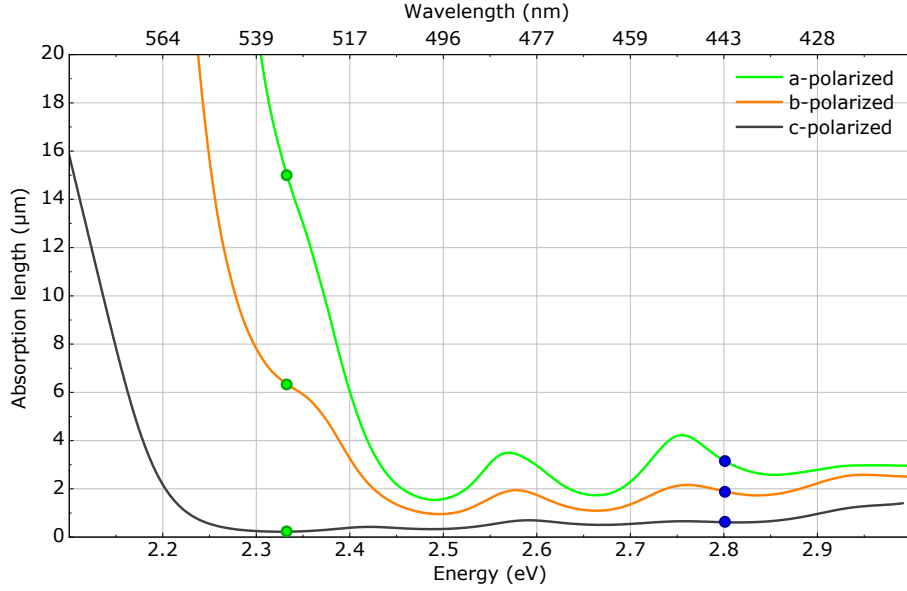
Figure 4.5: Absorption lengths for light polarized along three major crystallographic directions in a rubrene single crystal. Green circles correspond to a 532 nm excitation, blue circles—to 442 nm excitation.

because of the large relative strength of the c-polarized emission: the peak PL emission is about 20 times larger when detecting c-polarized PL (Fig. 4.3b,d) than when detecting b-polarized PL (Fig. 4.3a,c). Finally, the most striking differences are observed for c-polarized PL: the amplitude of the higher energy peak of the emission spectrum and its position are strongly dependent on the *excitation* polarization and wavelength (Fig. 4.3b,c). Some of these observations have been partially reported before [16, 18–24]. In particular, the shift of the PL band maximum from 2.19 eV to 2.16 eV when changing the polarization of the excitation light has been previously reported in Ref. [21], but without discussing it. A large variability of the observed PL spectra in the references above has lead to a number of inconsistent interpretations. I will discuss some of the existing interpretations in chapter 5, together with

a review of experimental artifacts that can modify the PL spectrum.

4.2 Intrinsic photoluminescence of rubrene

All the spectra in Fig. 4.3, and also all those reported in the literature to date, can be reconciled by taking into account the strong absorption anisotropy of rubrene single crystals. In the following, I show that all spectra originate from three intrinsic polarized emission spectra, which are then deformed by the choices of excitation and detection conditions. The most important effect that needs to be considered is the strong absorption of the intrinsic PL by the material itself, in particular for higher emission energies and for c-polarized emission, where the rubrene absorption is strongest. Using the absorption spectra that I presented in Fig. 3.4, I can calculate quantitatively the effects of absorption and re-absorption (a.k.a. self-absorption) on the PL emission spectra. They depend on the amount of overlap between photoluminescence and absorption spectra, and on the depth at which excitation occurs when compared to the absorption length of the emitted PL.

The amount of PL power detected in a direction normal to the surface is proportional to the amount of excitation light deposited at a given depth inside the crystal multiplied by the amount of PL light that can reach the surface of the crystal, and integrated over all depths. Hence, the detected spectrum $PL_d(\omega)$ is related to the intrinsic spectrum $PL(\omega)$ by

$$PL_d(\omega) = PL(\omega)\alpha \int_0^\infty e^{-\alpha x}e^{-\alpha(\omega)x}dx$$

$$= PL(\omega)\frac{\alpha}{\alpha + \alpha(\omega)} \tag{4.1}$$

where α is the absorption coefficient for the excitation light and $\alpha(\omega)$ is the absorption coefficient for the emitted PL. The intrinsic spectrum can be recovered from the measured one by multiplying it with $(1 + \alpha(\omega)/\alpha)$. Here, it is understood that one must use the absorption coefficient values for the given light polarization, as given by the appropriate absorption curve in Fig. 3.4. Figure 4.6 compares the change of the experimental c-polarized PL emission spectrum for different excitation polarizations with the evolution of the same spectrum as can be modeled using Eq. 4.1. It also shows a similar deformation of the emission spectrum (Fig. 3.4c) when measuring rubrene solutions with different concentrations. The real spectrum is measured at the lowest concentrations, while at higher concentrations an artificial red-shift of the emission peak occurs.

For the data in Fig. 4.6, I chose 532 nm (2.33 eV) for excitation, because at this photon energy the contrast between b- and c-polarized absorption constants is the largest (Fig. 3.4). Under these excitation conditions, the distortion of the PL spectrum is expected to be minimal for c-polarized excitation (PL originates close to surface), and maximal for pure b-polarized excitation (PL originates deeper inside the crystal). This can be clearly seen in Fig. 4.6a, where the spectrum excited by the b-polarized light is strongly attenuated in the higher-energy parts. The intrinsic PL emission spectrum can be obtained by applying Eq. 4.1 to the data
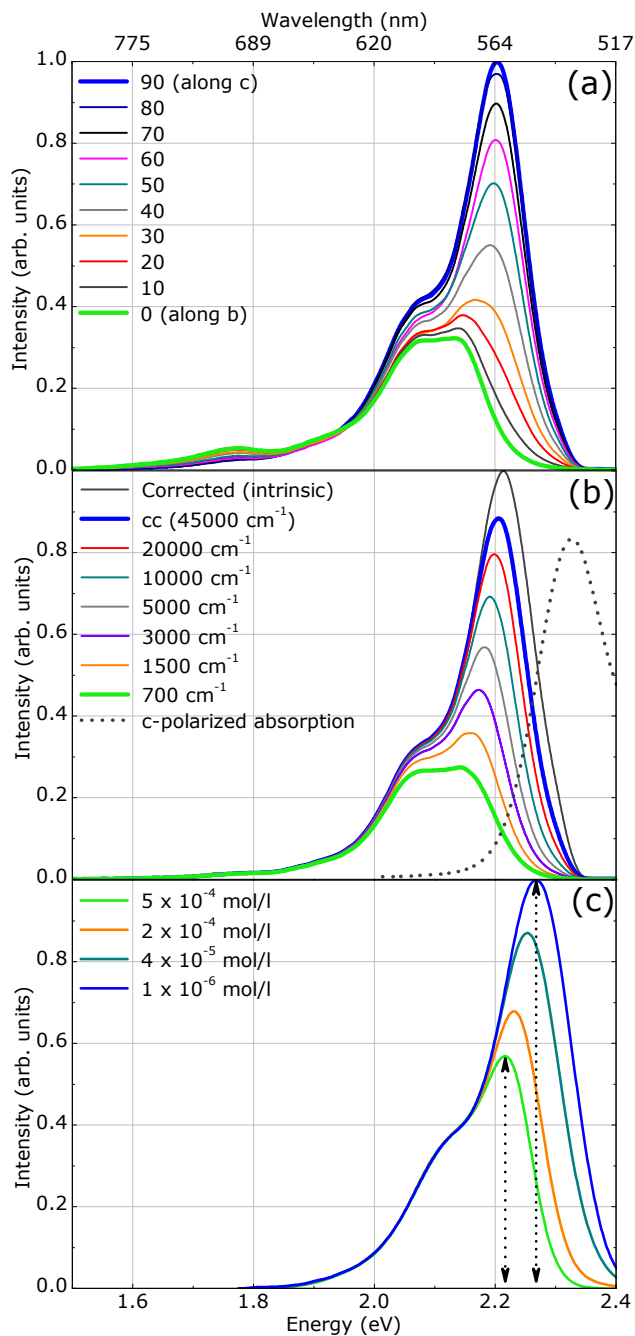
Figure 4.6: (a): Experimental photoluminescence spectra measured on bc facet of a rubrene single crystal with 532 nm excitation light polarized at various angles from the b-axis. (b): Modeling of reabsorption effect on the appearance of the photoluminescence spectra. (c): Effect of reabsorption on photoluminescence spectrum of rubrene in solution at various concentrations.

obtained with c-polarized excitation. From this, it is then possible to predict the behavior when rotating the excitation polarization towards the b-axis. This is done in Fig. 4.6b, which shows the intrinsic spectrum as well as the experimental spectrum obtained with c-polarized excitation and the spectra predicted for all other intermediate excitation polarizations. The evolution of the spectra matches the observed experimental behavior very well. However, the exact value of the absorption coefficient for b-polarized excitation light is very important to match the experimental results. Here I find that the experimental results are reproduced by assuming that the absorption coefficient for the excitation light at 532 nm (2.33 eV) is less than what was experimentally determined in Fig. 3.3b. I find that the b-polarized absorption coefficient must be $\alpha_b = 700 \ cm^{-1}$ instead of $1500 \ cm^{-1}$ to fit the PL emission data. This confirms that the measured b-polarized absorption spectrum is affected by leakage of the strong c-polarized absorption (see discussion above). In fact, the absorption coefficient $\alpha_b = 700 \ cm^{-1}$ at 2.33 eV that is needed to reproduce the effect of the excitation polarization on the PL spectrum is very close to the value of $\alpha_b = 400 \ cm^{-1}$ that can be assigned to the tail of higher energy bands. The small difference between these two values could be explained by an additional temperature-induced broadening of the absorption bands, which is present under CW laser excitation.

The procedure outlined above to analyze the PL emission spectra can be used to obtain the intrinsic PL emission spectra from the experimental data in Fig. 4.3. The results are shown in Fig. 4.7. The intrinsic spectra in this figure are derived from multiple experiments like those shown in Fig. 4.3 using Eq. 4.1 and the absorption spectra in Fig. 3.4. These intrinsic spectra do not depend on the excitation/detection

geometry, the wavelength or the polarization of the excitation. I confirmed this by using several wavelengths for the excitation from the UV to the visible spectral range (325 nm, 405 nm, 442 nm, 532 nm) and also by using a 1 picosecond pulsed laser at 488 nm.

4.3 Analysis of corrected intrinsic photoluminescence spectra

Following the same procedure used when analyzing the absorption spectrum, I modeled the intrinsic PL emission spectra presented in Fig. 4.7. Again, I took care of minimizing the number of fitting parameters, choosing a model function that uses a sum of identical Voigt profiles separated by the same energetic distance. Five Voigt profiles (FWHM is 0.13 eV, ratio between Gaussian and Lorentzian widths is 11) separated by 0.147 eV closely reproduce the intrinsic c-polarized photoluminescence spectrum of rubrene, with five bands centered at 2.22, 2.07, 1.92 and 1.78 and 1.63 eV (Fig. 4.8a). The intrinsic PL spectrum emitted by the ab facet of rubrene (Fig. 4.7b) can be accurately reproduced by a superposition of two progressions (Fig. 4.8b). The first progression consists of four bands centered at 2.04, 1.90 and 1.76 and 1.62 eV, separated by 0.140 eV. The second progression is identical to the one on Fig. 4.8a and corresponds to the one for c-polarized emission. (Dash-dotted lines in Fig. 4.8b. The lower energy bands are not shown because of their negligibly small amplitudes). The reason behind the presence of a replica of the c-polarized progression in the ab-polarized PL spectrum is again the "leakage" of the c-polarized emission with its very large relative intensity. A detailed discussion of this and other
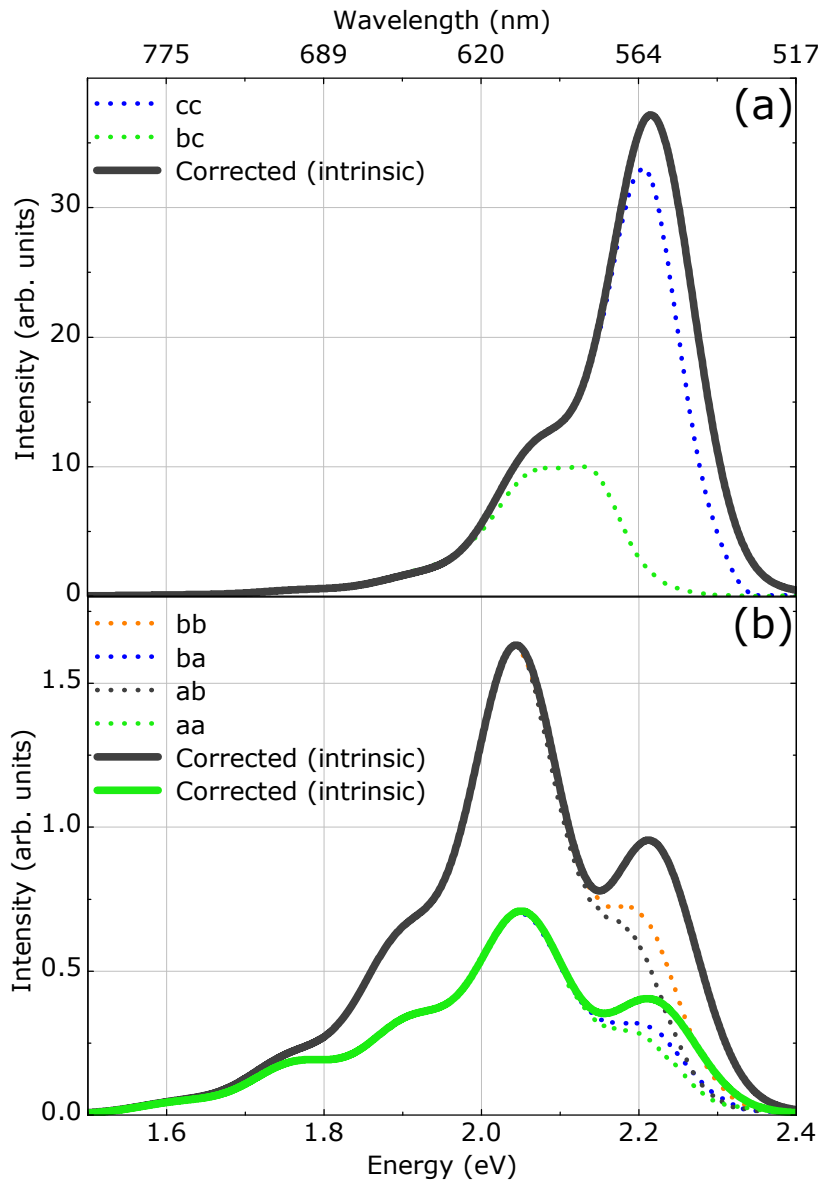
Figure 4.7: PL spectra for *c*-polarized emission (a) and for *ab*-polarized emission (b) of a rubrene single crystal with corresponding spectra corrected for reabsorption. The spectra were taken from *bc* (a) and *ab* (b) facets.
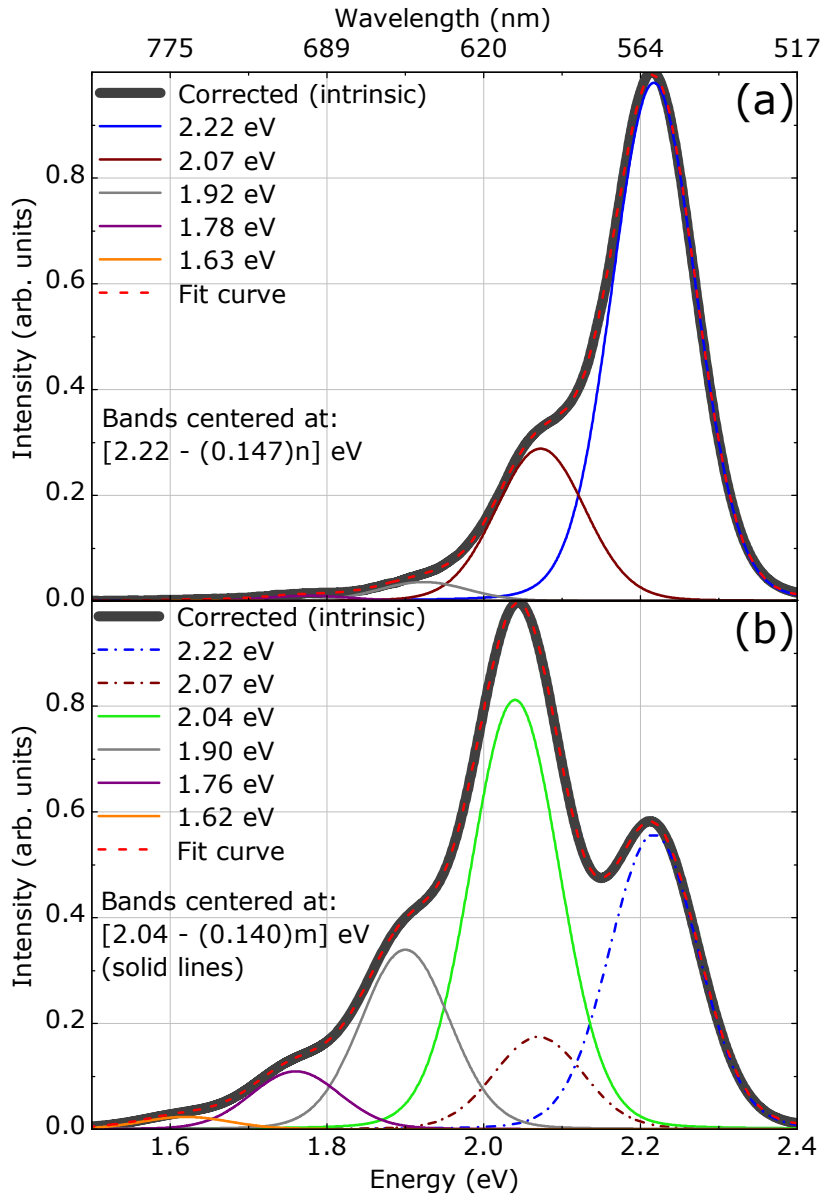
Figure 4.8: Peak fit of the corrected intrinsic photoluminescence spectra from the *bc* (a) and *ab* (b) facets.

artifacts affecting the experimental PL spectrum is given next.

Chapter 5

Experimental artifacts and data interpretation

5.1 Possible experimental artifacts

The most striking feature of the rubrene photoluminescence spectra is that the majority of the PL is emitted with c-polarization. The peak of the c-polarized emission is 20 times larger in intensity than the peak of the a- or b-polarized PL that can be detected from an ab facet. This large anisotropy in PL matches the large absorption anisotropy observed in Fig. 3.4.

When determining the PL spectrum of a rubrene crystal, the strong c-polarized emission can cause a number of experimental artifacts. This is particularly true when measuring as-grown rubrene crystals with large ab facets. Since most rubrene crystals are flat platelets with the surface perpendicular to the c-axis, upon excitation there will always be a very strong c-polarized emission that propagates away

from the excitation point in all directions parallel to the *ab*-surface. When capturing PL light into a small solid angle in a direction perpendicular to the *ab*-surface of the crystal, the amount of *c*-polarized light that is detected can be quite small. It will increase if the solid angle increases (detection from a closer distance, or with shorter focal length lens in a confocal geometry) or for small deviations from the perpendicular direction. In addition to this, the less absorbed spectral component (the long wavelength part) of the PL light propagating from the excitation point inside the flat crystal will be the one reaching the edges of the crystal. Detection of any light scattered from the edges of the crystal would then cause an artificial enhancement of the longer wavelength portion of the spectrum. Finally, micrometer-sized mechanical imperfections that are often present on the crystal surface can cause scattering of the *c*-polarized light present inside the crystal, and this effect will redirect the c-polarized light into the detection system. Thus, scattering by surface imperfections can give rise to the appearance of a strong PL band centered around 2.22 eV even in configurations where the detection system is nominally set up to detect *a*- or *b*-polarized light.

Figure 5.1 gives examples of spectra affected by all these artifacts, from the variations of the detected PL spectrum with numerical aperture of the detection system (Fig. 5.1a), to the variations when tilting the crystal (Fig. 5.1b), to the effect of scattering centers on the surface (Fig. 5.1c), and finally to the strong redshift of the spectra observed when detecting the light that has propagated a long way in a rubrene platelet (Fig. 5.1d).

The effect of imperfections at the crystal surface is particularly important when measuring PL spectra using a collimated laser beam with a relatively large cross

37

section. Under such circumstances, several micrometer-sized defects can be present in the illuminated area, and they will scatter some c-polarized light, creating a larger shoulder around 2.22 eV in the PL spectrum. I experimentally confirmed under the microscope that this effect is very strong (Fig. 5.1c), with any defect in the excitation area appearing as a bright source of yellow (2.22 eV) light on top of a dimmer orange (2.04 eV) photoluminescence. This effect explains the strong variability of the PL spectra obtained from different regions on the surface of the same rubrene crystal. With a good control over surface quality under the microscope, I observed a perfect reproducibility of the rubrene PL spectrum obtained from tens of crystals of various shapes and sizes. As expected, PL measurements from facets other than the naturally extended ab-facet ({001} surface) are not as sensitive to surface quality, but unfortunately, most PL studies reported to date in rubrene relied on PL collection from the ab facet, which is usually the largest one in as-grown crystals.

The dominance of the c-polarized PL emission and the effect of scattering centers on the surface can also be directly visualized thanks to the strong self-guiding of light in thin platelet-like crystals and thin crystalline films with extended ab-surfaces (Fig. 5.1d, inset). The majority of the radiated c-polarized PL lies within the critical angle for total internal reflection. As can be seen on the inset of Fig. 5.1d, it is guided from the excitation spot towards the edges, and is then scattered both at the edges and on its way to the edges by surface imperfections and cracks. At the same time, there is a strong reabsorption while the c-polarized light propagates away from the excitation spot, and only the longer wavelength portions of the emission reaches the edges of the crystal. I demonstrated this effect by illuminating an elongated rubrene
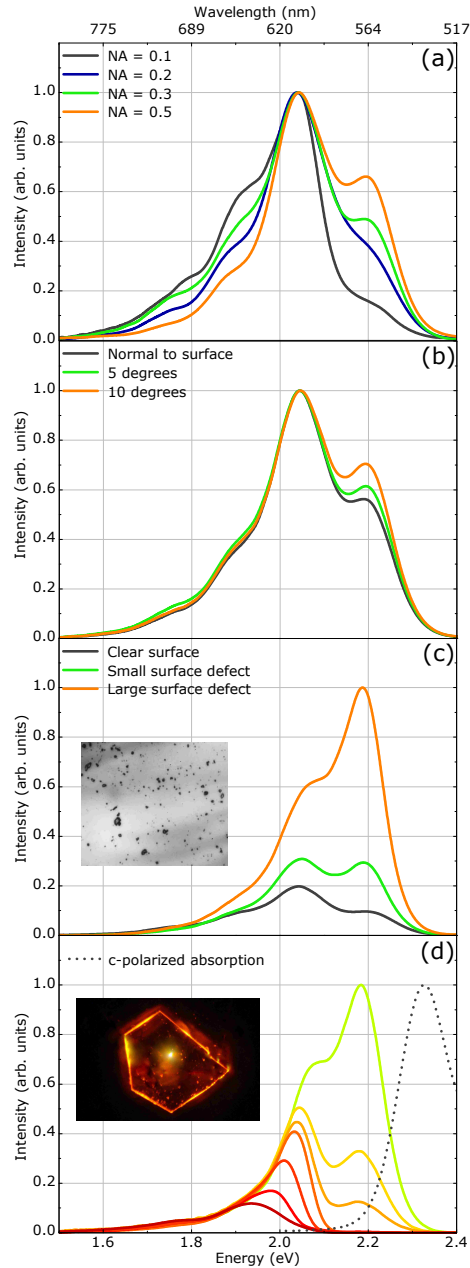
Figure 5.1: (a): PL spectra collected from *ab* facet with various numerical apertures. (b): PL spectra observed at various angles from the normal to the *ab* facet. (c): modification of the observed PL spectrum due to surface defects in the excitation/detection region. Inset: image of a surface of a rubrene crystal covering 90 x 60 micrometers (d): effect of reabsorption on the PL spectrum emitted from the edge of a crystal with illumination at various distances from the edge. Inset: waveguiding of light in thin platelets of rubrene.
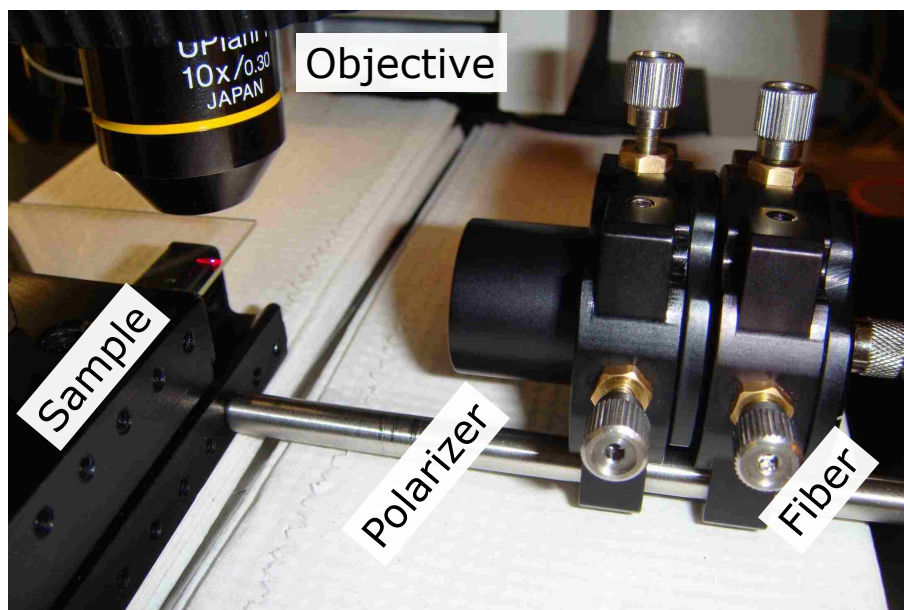
Figure 5.2: Experimental setup used to visualize the effect of reabsorption of waveguided PL light in a rubrene single crystal.

crystal at various distances from the edge, while collecting the photoluminescence from the edge with a fiber (Figure 5.2 and Figure 5.3). The evolution of the detected PL spectrum with increasing distance between the edge and the excitation spot is shown in Fig. 5.1d together with the normalized c-polarized absorption spectrum of rubrene. As can be seen in Figure 5.4, waveguided light can travel large distances in thin platelets of rubrene. An even more dramatic effect can be seen in tetracene (Fig. 5.5): due to a stronger overlap between absorption and emission spectra [29], waveguided light appears yellow, while intrinsic PL of tetracene is mostly green.

I have shown that the high-energy shoulder at 2.22 eV in the PL emission spectrum of rubrene obtained from *ab* facets is an artifact created by the leakage of the
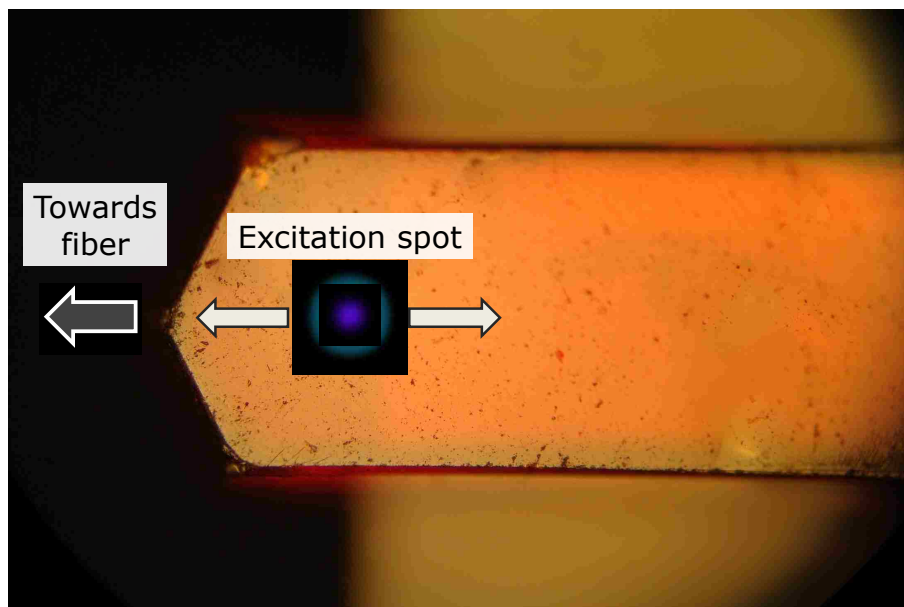
Figure 5.3: Elongated rubrene crystal from Figure 5.2 viewed through the microscope objective. Position of the excitation spot was varied in the shown range, while PL detection geometry remained fixed.

strong c-polarized luminescence typical of rubrene. It can be minimized by ensuring a good crystal surface quality, precise crystal alignment, and by reducing the numerical aperture of the PL detection. The dark grey curve in Fig. 5.1a is an example of almost perfect PL measurement from the ab facet. The presence of the "leaking" c-polarized progression is minimized here, which produces a slight relative enhancement of lower-energy b-polarized bands, because the spectra were normalized to their peak. A complete removal of this artifact is practically impossible, given the nature of the radiation pattern of the c-polarized dipole and its relative strength.
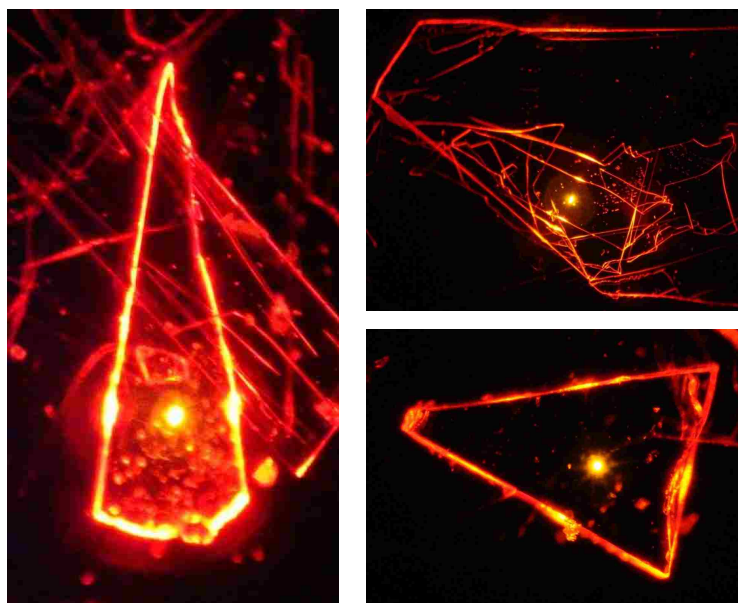
Figure 5.4: Waveguided photoluminescence in thin rubrene platelets.
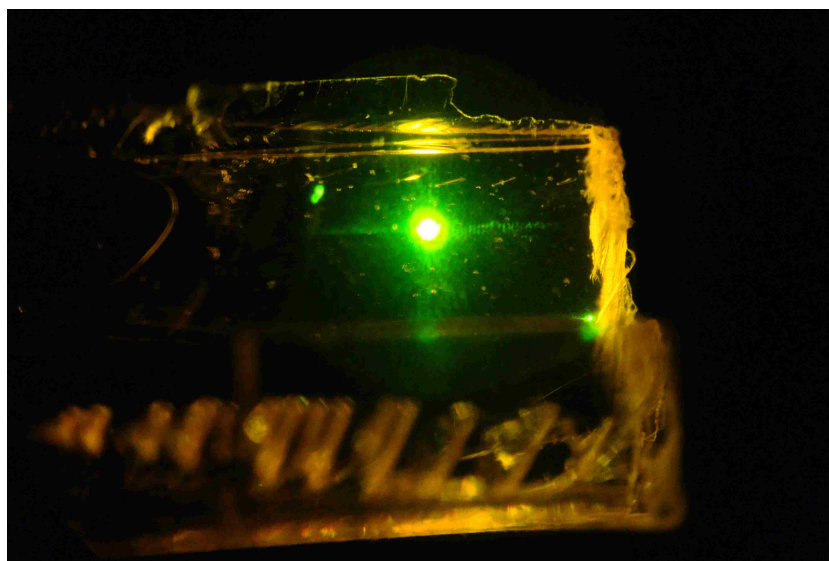
Figure 5.5: Reabsorption of waveguided photoluminescence in a tetracene single crystal. While the intrinsic PL of tetracene is green, waveguided PL, scattered by crystal edges, appears yellow due to reabsorption.

To summarize, highly anisotropic absorption and emission of rubrene single crystals, a strong reabsorption of the PL spectrum due to an overlap between PL and absorption curves, and a high sensitivity to the surface quality account for a large variability of the reported PL spectra in the literature. If the effects described above are not taken into account, the resulting spectra can be mistakenly measured red-shifted (reabsorption) and position-dependent (mechanical imperfections on surface). For example, in Ref. [19] a stronger high frequency band in the PL spectrum was observed in the presence of pyramidal structures on the ab surface of rubrene. This observation was interpreted as exciton confinement, while I show here that it must instead be related to scattering of c-polarized emission by the pyramidal structures on the surface. Ref. [16] compared PL spectra of rubrene solutions at different concentrations with rubrene powder and crystals. The observed shift in the PL peak position was attributed to an increased intermolecular interaction, while in reality it is mostly caused by reabsorption. Ref. [24] observed modifications in PL spectra of different polymorphs of rubrene microcrystals and proposed that "the remarkable difference in PL spectra might reflect a substantial change of exciton activities during relaxation". However, spectra obtained from different polymorphs of rubrene are expected to be affected by reabsorption to a different degree, and must be corrected for this artifact before a direct comparison can be made. Ref. [18] attributed a 60 nm shift of the crystal PL peak relative to solution to strong intermolecular interactions in crystalline rubrene, and Ref. [20] explained similar spectral variations as "the emission presumably occurs from significantly red-shifted states, e.g., luminescent traps". However, the observed variations can instead be assigned to the fact that the crystal PL spectrum was likely collected

from the *ab*-facet, and cannot be directly compared to the PL emission of rubrene in a solution, as discussed above.

Furthermore, PL spectra obtained in systems other than macroscopic single crystals are affected by the same experimental artifacts described above. Ref. [35, 36] present PL spectra of rubrene nanoparticles, while Ref. [37] discusses PL emission originated from rubrene nanowire arrays. While all presented spectra show visible variations, such variations are likely to originate from the same unique intrinsic spectrum, modified by circumstances of excitation/detection. Of course, precise modeling of reabsorption in the absence of perfect crystalline arrangement is complicated, especially given a lack of information on how the spectra were obtained. Still, I believe that the large observed variations in the published rubrene PL spectra are mostly caused by variations in the excitation/detection geometry, and are not directly caused by size-effects or morphology. Under most conditions, from the point of view of PL spectroscopy, rubrene single crystals behave like an oriented molecular gas of isolated rubrene molecules, which is consistent with the expected weak intermolecular interaction forces in molecular crystals. As I have shown, the optical spectra of a molecule in solution and of a single crystal are very similar (Fig. 3.3c), with the crystal spectrum retaining all main spectral features of individual molecules.

After having identified the most prominent high-energy bands in the PL emission spectrum of rubrene and how they can be affected by the experimental configuration of excitation and detection, I now discuss the lower energy PL bands. These bands can be seen in all the PL spectra that were reported above, near 1.92 and 1.78 eV, and are likely to be vibronic replicas of higher energy bands. At the same

44

time, enhanced PL bands at the same energies were reported and attributed to defect-related states that could originate from surface oxidation (see, for example, Refs. [21, 23, 38]). The precise origin and the reason behind the observed modifications of the rubrene PL spectrum at long wavelengths is still being debated, and some recent reports exclude oxygen as a reason for the 1.9 eV band enhancement [39]. I observe that the amplitude of the band at around 1.78 eV *slightly* saturates at higher excitation intensities (Fig. 5.7 a-b) and at higher temperatures (Fig. 5.7 c-d, accompanied by noticeable band broadening and overall PL intensity quenching). However, prolonged exposure to white light or laser emission in air did not result in any changes in the PL spectrum of high-quality stubby single crystals, and I observed a remarkable stability and reproducibility in the relative amplitudes of PL bands in tens of single crystals like those shown in Figure 2.3.

Some of the *thin crystalline films* of rubrene kept unprotected for a long time can develop a strongly altered PL spectrum, with strong low-energy bands dominating the spectrum, like the spectra reported in Refs. [16, 17, 25, 39]. An example of such a strongly altered spectrum is shown in Figure 5.6. I observed this altered PL emission to have a strong saturation behavior at higher excitation powers, which may be caused by a strong temperature dependence connected with laser heating. The amplitudes of the lower energy bands in this altered spectrum can also vary depending on the region of the crystal investigated, and the degree of alteration. The precise nature of this altered PL spectrum that peaks near 1.9 eV is not clear. In Ref. [25] a large difference between such a strongly altered PL spectrum of a rubrene single crystal and that of rubrene in solution was attributed to either oxidation, or a presence of amorphous inclusions in the crystal, following Ref. [39]. However,
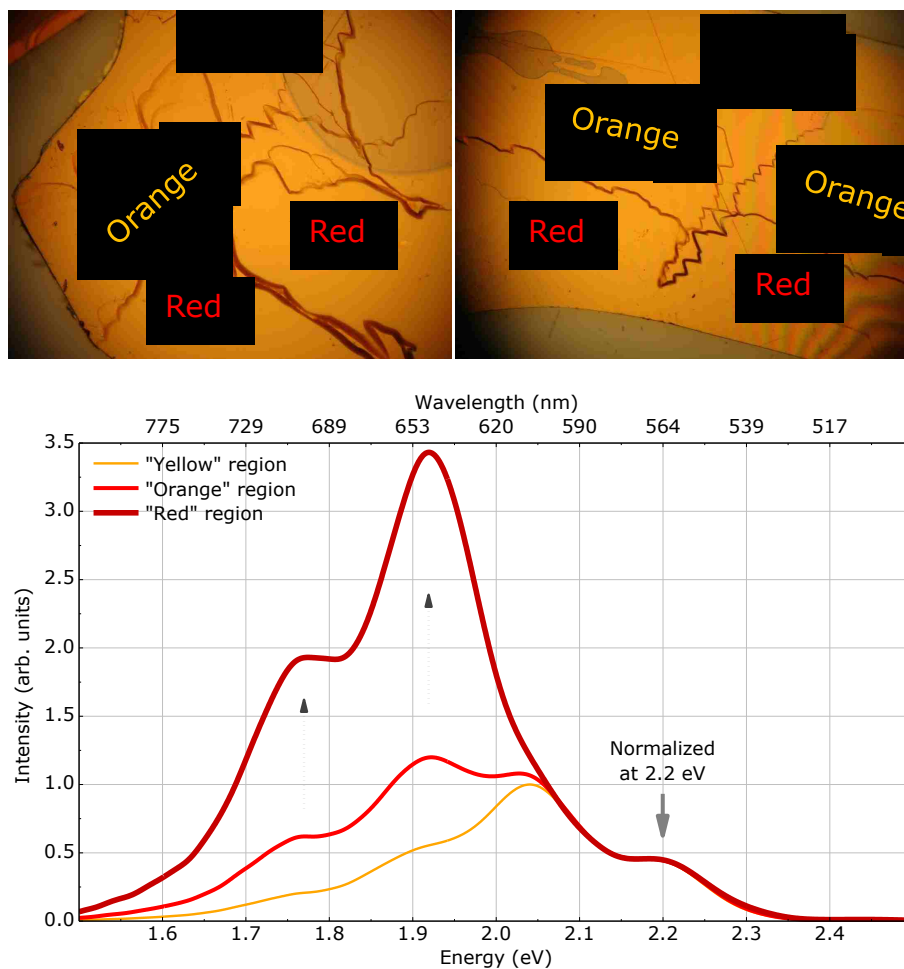
Figure 5.6: Top: regions in a rubrene sample possessing modified (to a different degree) PL spectrum: Bottom: PL spectra collected from different regions of the sample shown.

I have measured this altered spectrum to be *strongly polarized*, which indicates that its source remains *crystalline*. This would be consistent with Ref. [40] which demonstrated the formation of a crystalline rubrene peroxide layer above pristine rubrene crystalline domains. Still, the thickness of this oxidized layer would need to be relatively large to produce an observed strong modification to the PL spectrum.

Sometimes two phases (with normal and altered spectrum) can coexist inside the same sample, with sharp boundaries between domains that are sometimes visible under optical microscope (Figure 5.6, top). Regions with this altered spectrum have a noticeably higher PL quantum yield at low excitation powers). It must be noted that the PL bands that dominate this altered spectrum are near the possible vibronic replicas of the c-polarized PL spectrum of pristine rubrene that I have identified close to 1.78 and 1.92 eV. I observed that a solution prepared from a rubrene sample with altered PL spectrum possesses absorbance and PL spectra identical to that of pristine rubrene, which could indicate that the observed alterations are related to the changes in structure (morphology) rather than chemical content. Ref. [41] showed an appearance of a large peak in the density of trap states at 0.27 eV above the valence band after exposure of rubrene single crystals to oxygen and light, which would be energetically consistent with this strongly altered PL spectrum. On the other hand, Ref. [42,43] argue that the HOMO of oxidized rubrene has an energy ~ 1 eV lower than that of rubrene, and cannot account for the band gap acceptor state, and propose instead that the presence of oxidized molecules disturb the long range periodicity and the delocalized nature of the HOMO in the crystal, also acting like point defects that produce localized acceptor states and can reduce carrier mobility. This would agree well with my own observation of a reduction of exciton diffusion length (see Ref. [34] for the method used to determine the diffusion length and for pristine rubrene data) in rubrene samples with altered PL spectrum, but for the moment the available data does not allow any definitive conclusions.

To conclude this section dedicated to experimental artifacts, I repeat that typical distortions of the PL spectrum that have been reported in the literature are the

appearance of an abnormally strong band close to 2.2 eV when measuring normal to the *ab* surface, and a red-shift of the peak of the PL spectrum caused by reabsorption. In addition, in some rubrene samples one sometimes finds regions that display a strongly altered PL spectrum that peaks around 1.9 eV, but is not caused by reabsorption effects. The material modifications that give rise to this strongly altered spectrum are at present still an open question. Special care needs to be taken when selecting rubrene single crystals for experiments intended to reveal intrinsic properties of pristine rubrene. In particular, the unclear origin of the strongly altered PL spectrum peaking near 1.9 eV, observed in Refs. [16, 17, 25, 39], casts doubts on the interpretation of measurements, like those in Ref. [25], that have been performed on crystals characterized by this altered PL spectrum that does not correspond to pristine orthorhombic rubrene.

5.2   Theoretical model

Figure 5.8 shows a summary of the intrinsic absorption and emission spectra of rubrene. Fig. 5.8a reproduces the *c*-polarized absorption and emission spectrum from Fig. 3.4c and Fig. 4.8a. Figure 5.8b shows the *ab*-polarized absorption and emission spectrum of rubrene, as it can be obtained from the experimental spectrum of Fig. 3.4a-b and Fig. 4.8b when eliminating the spectral components at 2.32 eV (absorption) and 2.22 eV (emission) that I have assigned to leakage of the c-polarized spectrum. Figure 5.8c shows the absorption/emission of amorphous rubrene, which I obtained by melting rubrene in an enclosure protected from atmospheric influences.

To understand the final intrinsic absorption and emission spectra presented in
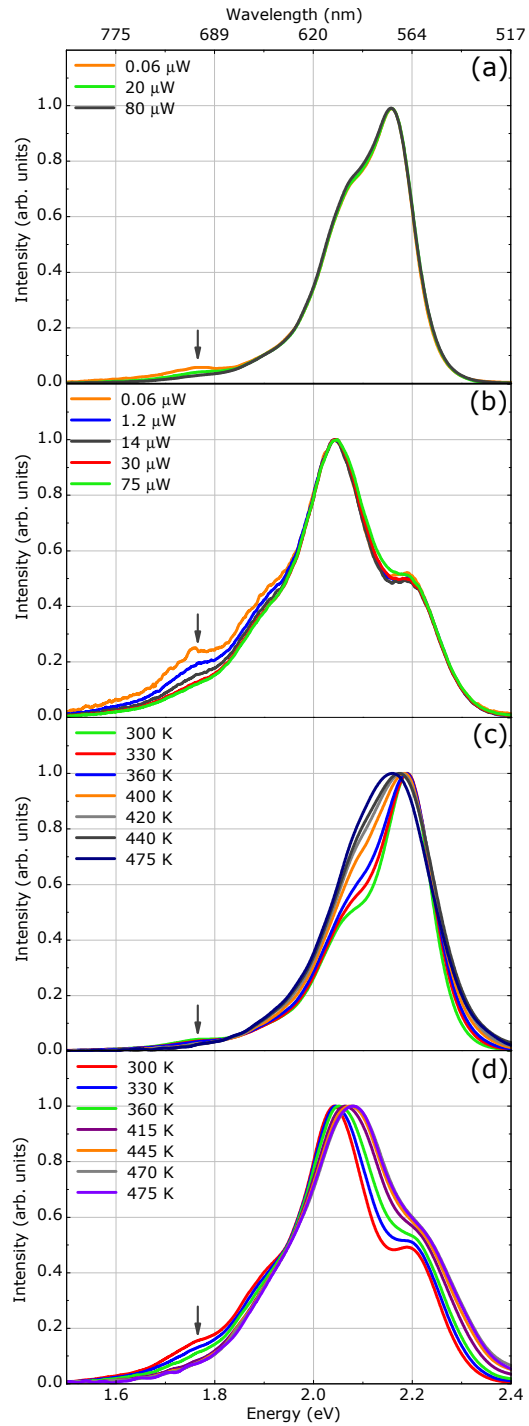
Figure 5.7: Normalized photoluminescence spectra collected from the bc (a) and ab (b) facet at various excitation powers. Normalized photoluminescence spectra collected from bc (c) and ab (d) facets at various temperatures.
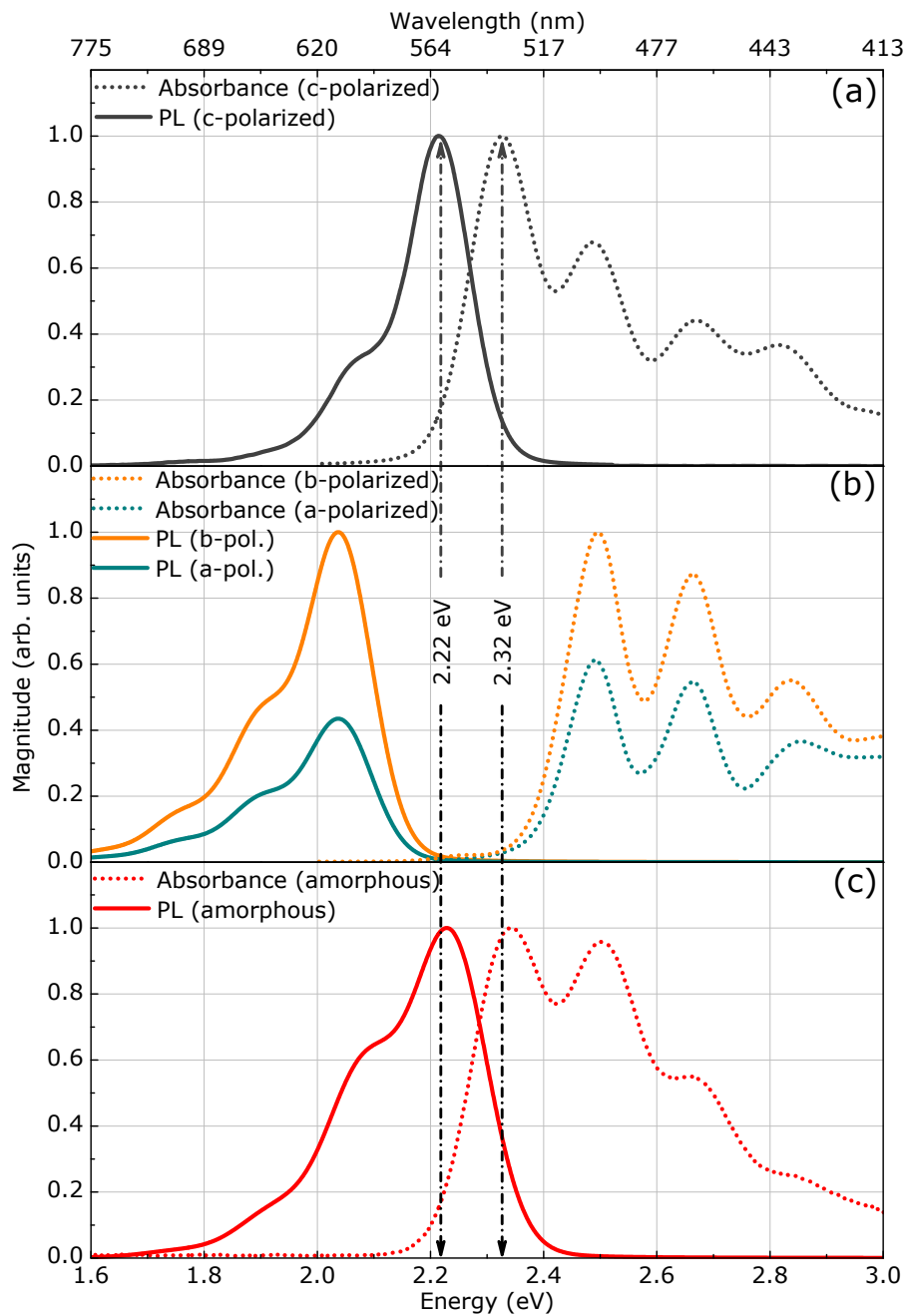
Figure 5.8: Intrinsic polarized absorbance and photoluminescence spectra of rubrene single crystals. (b) shows the correct ratio between a- and b-polarized absorption ans PL emission strengths.

Figure 5.8, I first recall the expectations for the rubrene molecule as found in the rubrene crystal, which has a C_{2h} symmetry with a twofold rotational symmetry along the M-axis and a mirror plane perpendicular to it [27].

Quantum chemistry computations predict that the first optical absorption corresponding to the lowest energy HOMO-LUMO transition in the rubrene molecule occurs around 2.3 eV, coupling only to light linearly polarized along the M-axis [32]. The next higher electronic transition is predicted to be around 0.3-0.55 eV higher in energy, to be much weaker, and to couple to light linearly polarized perpendicular to the M-axis. The first HOMO-LUMO transition in the rubrene molecule, which is M-polarized, directly maps to c-polarized absorption in the rubrene crystal, where all molecules have their M-axis exactly parallel to the c-direction [27]. In fact, the c-polarized absorption spectrum as seen in Figure 5.8a has a strong lowest energy absorption peak at 2.32 eV, and so does the spectrum of amorphous rubrene, where the M-axis will again dominate the optical properties. This first absorption peak at 2.32 eV can be assigned to a transition from the lowest vibrational state of the ground state to the lowest vibrational state of the first electronic excited state, while the higher energy peaks can be assigned to excitation to higher vibrational levels, building a vibronic progression. This is consistent with the fact that no other c-polarized absorption is expected below 3 eV. The c-polarized PL spectrum also agrees with this picture, with a highest energy emission at 2.22 eV, that can be understood as a transition from lowest vibrational state of the excited state to the lowest vibrational state of the ground state, followed by a rapidly decaying vibronic progression that corresponds to transitions to higher vibrational levels of the ground state.

The c-polarized absorption-emission spectrum of rubrene is qualitatively similar to that of other aromatic crystals such as tetracene. The larger Stokes shift of 0.10 eV in rubrene when compared to tetracene can be assigned to the larger number of lower frequency vibrational modes of the rubrene molecule [29]. The distances in the vibronic progressions (0.17 eV in absorption, 0.15 eV in emission) corresponds to the frequency of vibrational modes involving the stretching of carbon-carbon bonds [29, 44]. From the point of view of carbon-carbon stretching vibrations, the absorption/emission transitions at 2.32/2.22 eV can be considered "zero-phonon" transitions. In addition to the peaks of the vibronic progression, I have noted before that the c-polarized absorption spectrum has an observable additional absorption located at around 2.8 eV and with a width of about 0.25 eV (FWHM). This matches to the quasi-particle absorption edge as predicted by Sai et al. [32]. A similar enhancement in the c-polarized absorption around 2.8 eV has also been seen by Tavazzi et al. [33].

The a- or b-polarized absorption of rubrene is much weaker (by a factor of 7 and 4 peak to peak) than the c-polarized absorption. The spectra for both polarizations are very similar to each other and, once corrected for possible admixture of c-polarized absorption caused by experimental factors, are characterized by a first strong absorption peak at 2.49 eV, followed by a vibronic progression of decreasing strength until the spectrum starts being strongly influenced by the low-energy tail of the second electronic excited state with peak absorption near 3.7 eV (which couples to LN polarized radiation in the molecule reference frame and hence to ab polarized radiation in the crystal reference frame). The ab polarized emission spectrum is a reflection of the corresponding absorption spectrum. Here, too, a small band close

to 2.22 eV is most likely caused by an experimentally difficult-to-control leakage of c-polarized emission. In this view, the highest energy emission peak is observed at 2.04 eV, followed by a vibronic progression separated by 0.14 eV.

The ab-polarized absorption and emission as seen in Figure 5.8 cannot be assigned to a transition between ground state and an electronic excited state that has a transition dipole moment with components along the a- or b- axis of the crystal (LN axes of the molecule). First of all, the predicted oscillator strength for the second available electronic excited state in rubrene with an LN transition dipole moment is very weak [32]. Secondly, the excitation energy predicted for this transition is clearly larger than the observed first ab-polarized absorption peak at 2.49 eV. The calculated electronic transitions of the rubrene molecule (using TDDFT at B3LYP/6-31G level of theory as well as using the Zerner INDO (ZINDO) method [45, 46] as implemented in GAUSSIAN 03 [47]) give no dipole-allowed transition beyond HOMO-LUMO is predicted at energies matching the onset of the ab-polarized absorption. It should also be noted that the ab-polarized absorption peaks and their vibronic progressions accurately match the higher vibrational peaks in the c-polarized spectrum. It would be difficult to discount this as a coincidence. I therefore propose, in contradiction with the hypothesis of Tavazzi et al. [17], but consistently with the calculations of Sai et al. [32], that the first ab-polarized absorption peak cannot be assigned to a second electronic transition in the rubrene molecule.

I propose here that the ab-polarized absorption and emission in the rubrene single crystal must be due to a depolarization induced by molecular vibrations of the first M-oriented excitation. This vibronically induced depolarization of the HOMO-LUMO transition can be understood as the interaction of the $A_g \leftrightarrow A_u$ electronic

excitation with a vibrational mode, with appropriate symmetry, of the ground state (for emission) or of the excited state (for absorption). Similarly to the previous discussion of electronic states, the C_{2h} symmetry of the molecules in the rubrene crystal allows vibrational modes with four symmetry types: a_g, a_u, b_g, and b_u (I use lower-case letters to distinguish from the symmetry of electronic states, represented by capital letters). Starting from the vibrationless $A_g \rightarrow A_u$ transition of the molecule, which is entirely c-polarized in a crystal with rigid molecules, one can see that a dipole excitation to the A_u state that is in some b_g vibrational mode would be LN polarized. Recalling that the (L, N, M) components of the dipole operator in the C_{2h} point group transform as (B_u, B_u, A_u), it is easy to see that the dipole operator components along L or N, which have B_u symmetry, can create a transition between the A_g ground state and an excited state vibrational mode that has symmetry b_g: $A_g \otimes B_u \otimes (A_u \otimes b_g) = A_g$. On the other hand, excitations to some a_g vibrational mode of the excited state can be induced by a dipole operator component along M, which has symmetry A_u: $A_g \otimes A_u \otimes (A_u \otimes a_g) = A_g$. An analogous argument can be made for PL transitions. It follows that the ab-polarized vibrational progression in the crystal's absorption-emission spectra can be caused by transitions to higher vibrational modes that have symmetry b_g, while the vibronic progression in the c-polarized absorption-emission spectra can be caused by transitions to higher vibrational states with a_g symmetry. If the a_g and b_g modes have similar frequencies, then the c-polarized and the ab-polarized peaks would have almost the same position in the spectra, but the vibrationless transition would only be observed in the c-polarized spectrum. This is exactly what is seen in the absorption spectra of Figure 5.8. The vibrationless HOMO-LUMO transition is only observed in the

c-polarized spectra, while as soon as a transition is to a higher vibrational state, then it can couple to *ab*-polarized light.

The totally symmetric vibrational mode of the excited state responsible for the vibrational progression in absorption is likely the one calculated at 1331 cm^{-1} (0.165 eV) in Ref. [29], which has the largest normal coordinate displacement. Ground state vibrational modes with appropriate symmetry, which could be responsible for the vibrational progressions observed in the PL spectra, have been seen in the Raman measurements of Ref. [44] near 1163 cm^{-1} (0.144 eV).

Chapter 6

Exciton diffusion

6.1   Motivation and state of the art

Intermolecular forces in organic molecular crystals are generally much weaker than the forces inside of the molecules, hence many properties of the molecule are altered only slightly if one incorporates a molecule into a crystal [48]. For many problems, such crystal is nothing more than a framework that fixed oriented molecules in space without changing the molecules too much. It is common to make use of such a crystalline state in all kind of investigations where one needs molecules of known orientation. One example is the measurement of the symmetry of different excited molecular levels using polarized absorption and fluorescence spectra. From such measurements it became clear that the oriented gas model is too simple. In order to understand the electronic spectra of organic crystals one has to take into account the interaction between the molecules, and the interaction between an excited molecule with its originally unexcited surroundings. The result of this process is a breakdown

of the oriented gas model. Energy cannot be localized on one molecule during its whole lifetime in the excited state. The question that I try to answer is: how far and how fast can excitation energy migrate in molecular single crystals?

Since an exciton is a mobile, nonconducting, excited state of a crystal, its net displacement (diffusion length) during its lifetime is a very *fundamental property*. Fundamental studies of exciton dynamics in organic crystals are important for understanding the role of intermolecular interactions in exciton transport, and are of prime interest towards the optimization of photocarrier generation in organic photovoltaics, where exciton diffusion is a key process limiting the photovoltaic efficiency [49, 50]. However, direct experimental observations of exciton diffusion have proven difficult, and most available data was obtained by indirect methods [51–53], resulting in a relatively large variability between the reported diffusion lengths for the same materials [54, 55].

The experimental investigation of exciton diffusion is a challenging task especially in disordered molecular materials, where the exciton diffusion length is very short, of the order of a few tens of nanometers [50, 56, 57]. Organic molecular crystals with their intrinsic order, on the other hand, should allow for longer-range diffusion, and are also attractive for fundamental investigations. In fact, initial estimates put diffusion lengths in molecular crystals in the range of a few micrometers. Early work done in anthracene, mostly using indirect methods, claimed diffusion lengths of up to 30 μm [51–53]. Literature on other crystals such as tetracene or rubrene is also limited [54, 55, 58, 59]. In particular, the rubrene crystal has several compelling properties, including one of the highest room-temperature charge carrier mobilities ever observed in an organic material ($\sim$ 10-40 cm^{2}V^{-1}s^{-1} for holes in field-effect

transistors [4, 9–12]) and a high photoconductivity [13, 14]. In addition, recent photoconductivity studies in rubrene [59] have been interpreted in terms of long exciton diffusion lengths of several micrometers that would allow excitons to migrate to the crystal surface, but no direct observations of exciton diffusion in rubrene have been reported yet. Motivated by the importance of exciton migration for the photoconductivity process and by the interest of rubrene as a material for optoelectronics, a direct imaging technique to observe exciton diffusion was developed.

6.2 Direct imaging technique

I visualize the presence of excitons and their diffusion by imaging the photoluminescence (PL) that originates from their radiative recombination after localized photoexcitation at well defined crystal surfaces. This straightforward method provides direct, intuitive images of the spatial exciton distribution. Some of its principles have been previously applied in inorganic semiconductors [60], but only under challenging cryogenic conditions required by the low binding energy of excitons. Thanks to the large excitonic binding energies in molecular crystals, I have succeeded in creating the experimental conditions that allow direct imaging of exciton diffusion at room temperature.

The experimental setup is described in Fig. 6.1. I create a localized distribution of excitons in a thin surface layer via a collimated continuous wave laser beam with a wavelength in the high absorption region of rubrene that is focused on the sample by a microscope objective. The same microscope objective images the surface of the sample onto a CCD camera. By using appropriate filters, I can photograph both
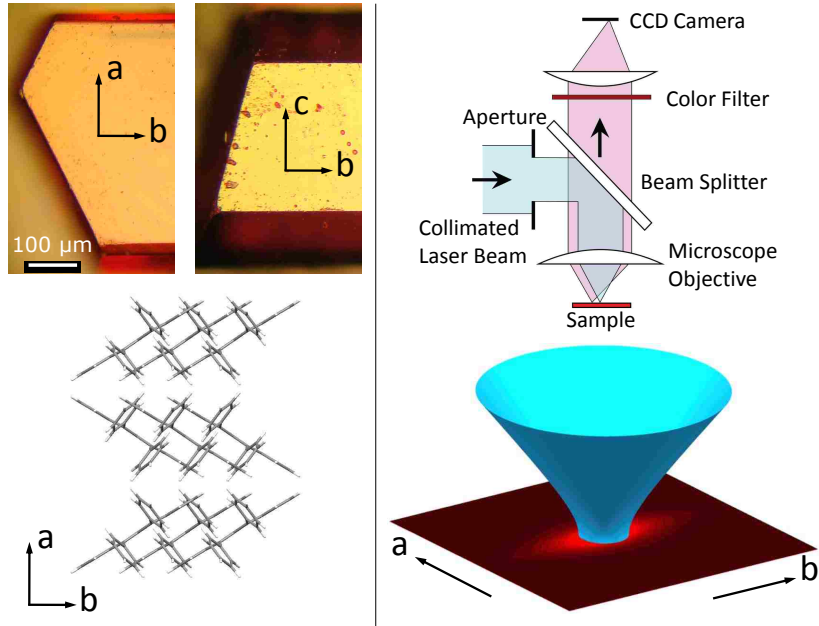
Figure 6.1: Top-left: *ab* and *bc* facets of rubrene single crystals. Bottom-left: molecular packing in the crystal and definition of crystallographic axes. Top-Right: experimental configuration. Bottom-right: scheme of the illumination conditions at the surface of the crystal.

the excitation light distribution and the PL distribution on the surface of a sample.

I use a well-corrected, variable numerical aperture infinite conjugate microscope objective to obtain an optimum combination of illumination profile, depth of field ($\sim 2\,\mu$m), and lateral resolution ($\sim 0.5\,\mu$m). A small amount of truncation results in the excitation light intensity being a hybrid between an Airy pattern and a Gaussian distribution. The spot size is 1.1 μm, defined as the diameter at which the intensity falls to $1/e^2$ of its peak value. Fig. 6.1 (bottom-right) is a schematic view of the excitation beam focused on the sample surface and the PL pattern it generates.

Fig. 6.2 shows the intensity distribution of the excitation light and of the PL as I typically observe at the surface of all rubrene samples I studied. Independently

of the shape, size, orientation, or thickness of a crystal, as long as a surface that contains the b-axis is illuminated, I observe a pattern like that in Fig. 6.2. While the excitation is perfectly round and symmetric, the PL is clearly elongated along the b-axis of the crystal, corresponding to a highly anisotropic exciton diffusion.

The significantly higher exciton mobility in the b-direction correlates well with the high charge carrier mobility observed in the same direction [4,9–12].

For the b-direction, it was possible to follow the decay of the photoluminescence intensity over three orders of magnitude for increasing distances from the center of the illumination. Fig. 6.2 shows the spatial dependence along the b-axis for both excitation light intensity and PL intensity taken using five different samples. The excitation and emission profiles are normalized to the same level at the center of the illumination. The excitation light decays very rapidly as highlighted by the semilogarithmic scale in the plot, but the photoluminescence extends over much larger distances.

The reproducibility of the data from all five samples shown in the figure is very good, and the spatial dependence at larger distances from the center can be fitted for all samples simultaneously by an exponential function $\exp(-x/d)$, where x is the distance from the center of the excitation spot and $d = 2.0 \pm 0.2$ μm.

The data in Fig. 6.2 was taken at a laser power of 10 nW, which still gives a good signal-to-noise ratio while avoiding overexposure of the crystal. This power corresponds to a flux of $\sim$ 20 photons per nanosecond incident on the 1.1 μm diameter spot and absorbed with an exponential absorption length of 2.0 μm. This gives an absorbed photon rate of $\sim$ 10 photons ns$^{-1}\mu$m^{-3}. Photon absorption results in a singlet molecular exciton with a lifetime of less than 10 ns [13, 14], meaning
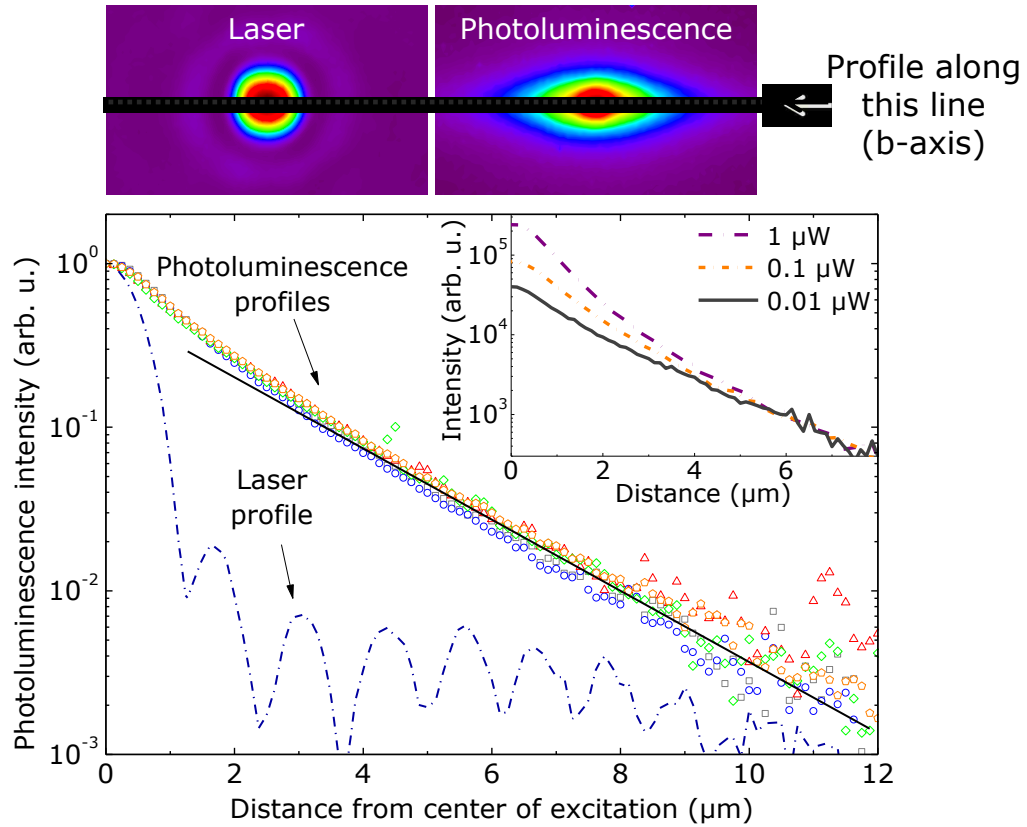
Figure 6.2: Top: contour plot of the intensity distribution of the excitation light and of the photoluminescence at the surface of a rubrene sample. Bottom: intensity of the excitation light and intensity of the photoluminescence emitted by the diffusing excitons versus the distance from the center of the excitation spot along the b-axis of the crystal. The photoluminescence data belongs to five different crystals, represented by different colors. Inset: Normalized photoluminescence profiles obtained at different excitation laser powers.

that at any given time there are less than 100 μm^{-3} singlets in the excitation spot. This corresponds to a singlet exciton for every ten million rubrene molecules, and shows that the exposure conditions remain a relatively small perturbation.

6.3 Theoretical model and data interpretation

I now turn to the discussion of how the data above should be interpreted. Measurements of the PL time-dynamics in rubrene have shown that an initial fast photoluminescence decay that happens in less than 10 ns is followed by a relatively strong PL that decays much more slowly [13, 14, 61]. This indicates that directly photoexcited singlet excitons have a lifetime of less than 10 ns and that many of them undergo fission [3, 62] to create longer lived triplet excitons. The PL seen at later times is then the result of triplets interacting with each other and fusing, pooling their energy to re-create a singlet exciton, which subsequently radiatively decays [3]. Even though the PL is always caused by the radiative decay of zero-momentum singlets, this effect makes it possible to detect the density of triplet excitons. Because of the large diffusion anisotropy, I can describe the spatial dependence of the triplet density T with the following one-dimensional diffusion equation:

$$\frac{d}{dt}T = G + D\frac{d^2}{dx^2}T - \frac{T}{\tau_T} - \gamma T^2, \tag{6.1}$$

where x is the coordinate along the b-direction, G represents the source function for the creation of triplet excitons (directly given by the excitation profile), D is the diffusion constant along the b-axis, and the last two terms on the right-hand side take into account the triplet lifetime τ_T (dominant at low triplet densities) and triplet-triplet collisions (dominant at high densities). The solution of the above diffusion equation in steady state and at low triplet densities far away from the excitation region — where the last term on the right-hand has a negligible influence on the triplet exciton density — is $T(x) = T_0 \exp(-x/L_D)$, with the diffusion length

$L_D = \sqrt{\tau_T D}$, the typical solution valid for any diffusion process of particles with a limited lifetime.

The spatially exponential PL decay in Fig. 6.2 can thus be assigned to an exponentially decaying density of triplet excitons, at densities where triplet-triplet interaction still provides for the PL by re-creating singlet excitons, but where the term T/τ_T is dominant in Eq. 6.1 [3].

Under these conditions, the PL intensity, given by the rate of decay of singlet excitons, is proportional to the rate at which singlet excitons are formed from triplets, and is therefore proportional to the *square* of the triplet density [3]. This means that the spatial exponential decay in Fig. 6.2, with an spatial exponential decay constant of 2.0 ± 0.2 μm, corresponds to a *triplet exciton diffusion length $L_D = 4.0 \pm 0.4$ μm.*

It was confirmed that the crystal surface has no effect on the observed diffusion by varying the excitation wavelength between 442 nm and 532 nm and showing that the corresponding change in the depth of exciton generation does not influence the PL pattern, as long as the depth of field of the detection is comparable with the excitation light absorption length. In addition, I have also obtained the same PL pattern when the sample surface was coated with fomblin oil. The observed long-range diffusion must be an intrinsic property of rubrene.

The interpretation of the observed long-range diffusion as triplet diffusion is also supported by my observation that an increase in illumination power, and thus of exciton density, leads to a PL intensity distribution that is disproportionally higher close to the center of the excitation spot, and to a transition to a pure exponential decay that happens at larger distances (Fig. 6.2, inset). Such behavior is consistent with the non-exponential spatial decay of the triplet density that is predicted by Eq.

6.1 at higher densities. There could also be a contribution of PL emitted directly by photoexcited singlet excitons, but further experiments will be needed to determine the role of singlet exciton diffusion, if any.

The large diffusion length along the b-axis that I observed is likely related to the molecular arrangement that forms stacks of molecules in the b-direction [27, 63], and that is also responsible for the exceptionally high hole mobility observed in the same crystallographic direction [4, 9–12].

6.4 Discussion of the flexibility of the technique

An example that further illustrates the flexibility of the exciton imaging technique that was described above is shown in Fig. 6.3. It shows (bottom-right) the intensity distribution of the PL obtained in a sample consisting of a ~ 1 μm thin rubrene crystal that spontaneously grew on the bc-facet of a larger rubrene crystal, but with its b-axis at an angle to the b-axis of the larger crystal below it. Performing the exciton diffusion experiment in such a system creates excitons both inside the small thin crystal as well as inside the large crystal below it. Independent diffusion of the two exciton populations leads to a PL distribution that is clearly a superposition of *two* independent ovals (Fig. 6.3, bottom-right), one belonging to the excitons that diffuse inside the small crystal, and one belonging to the excitons inside the larger crystal. The elongations in the PL pattern match the orientation of the two b-axes in the two crystals. In addition, I obtained PL patterns from several facets of rubrene microcrystals [31] where the b-axis was not parallel to the surface. Fig. 6.3 (third panel in the bottom) shows an example of what happens in this case. The
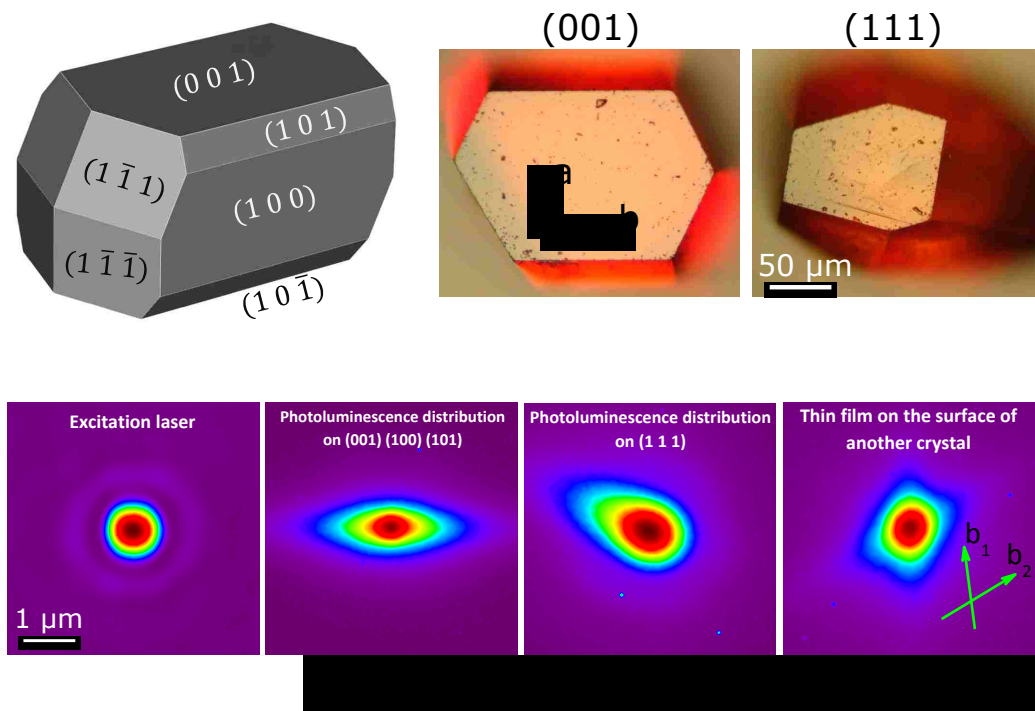
Figure 6.3: Top: Simulated habit of a rubrene single crystal (left); crystal facets where exciton diffusion experiments were performed (right). Bottom: contour plots of excitation light and photoluminescence intensity distributions corresponding to different experimental conditions. All contour plots cover an area of $5 \times 5 \ \mu m^2$.

asymmetry of the pattern obtained is caused by excitons that diffuse along the *b*-axis, but immediately reach the surface in one direction while they go deeper into the crystal in the other direction.

As these examples demonstrate, an important and attractive characteristic of the imaging technique that was demonstrated is its directness. It is flexible, it can be readily used under different experimental conditions (in a wide temperature range, inside of a cryostat, etc.), and it allows to establish the presence of exciton diffusion

as long as the diffusion length is at least larger than the optical resolution of the imaging system.

6.5 Conclusions

In conclusion, I described a direct imaging technique used to observe exciton diffusion and exciton mobility anisotropy in molecular crystals, and have determined a triplet diffusion length of 4 ± 0.4 μm along the b-axis of rubrene molecular single crystals. This imaging technique enables the investigation of exciton diffusion under different experimental conditions and in different materials, opening the doors to extensive new investigations of exciton diffusion phenomena, and ultimately providing important new knowledge on exciton transport processes in organic molecular crystals.

Chapter 7

Additional experiments, preliminary results, conclusions, and outlook

7.1 Two-photon spectroscopy of the rubrene single crystal

The goal here is to determine experimentally the electronic states that can be reached via two-photon absorption in rubrene single crystals. Two-photon absorption (2PA) is the process by which a molecule or material absorbs a pair of photons, the sum of whose energy equals the transition energy [64]. Thus, 2PA spectroscopy can be used as a tool to probe molecular properties, for example, the energy of the two-photon active excited states. This information can be different from, and complementary to, what is obtainable from one-photon absorption (1PA) spectroscopy;

the selection rules for 2PA are different from those for 1PA specifically in a system with an inversion center, where transitions are two-photon allowed only if they connect states with the same symmetry with respect to the inversion operation. Thus, if the ground state is of gerade (even) symmetry, only other gerade states can be reached by a 2PA transition, whereas ungerade (odd) states are one-photon allowed.

The most commonly used indirect technique is the two-photon-induced fluorescence (2PIF) method. Here, the intensity of the fluorescence emission induced by 2PA is measured irrespective of the final state reached by 2PA, because a molecule relaxes quickly (typically within about 1 ps) to the lowest vibronic level of the first excited state by internal conversion, and from this state radiative or nonradiative relaxation to the ground state can take place (with a characteristic lifetime). By monitoring the intensity of this fluorescence signal, it is possible to obtain relative or absolute 2PA spectra, depending on what information is available on the emission properties of the material, the spatial and temporal characteristics of the excitation beam, and calibration of the detection system.

For this experiment, I used b-polarized illumination of a rubrene single crystal at 840 nm utilizing the output of a Light Conversion TOPAS traveling wave optical parametric amplifier system pumped by a Clark-MXR laser system that delivered 1ps-duration optical pulses at a repetition rate of 1 kHz. Laser emission was focused on the ab surface of a thin rubrene crystal by a $10\times$ microscope objective. In this configuration, the Rayleigh range of the laser beam (100 μm) was much larger than the crystal thickness of 13.5 μm, that provided a nearly constant beam diameter inside the sample, and simplified further data interpretation.
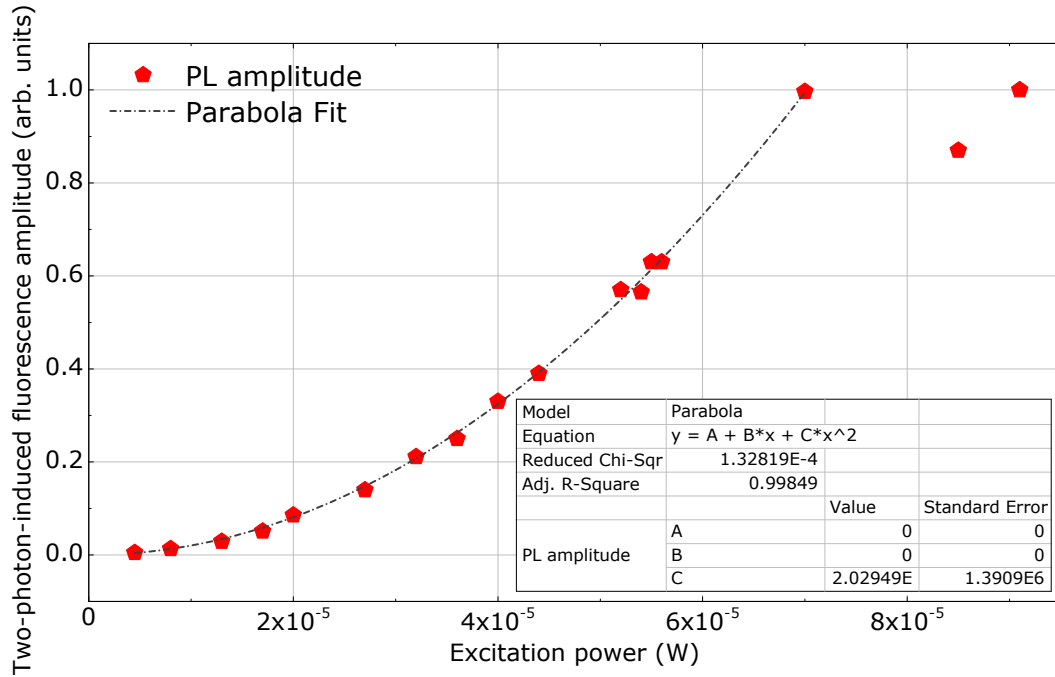
Figure 7.1: 2PA-induced fluorescence intensity versus excitation power. Inset shows fit parameters for the quadratic function used to approximate the experimental data.

Figure 7.1 shows the excitation power dependence of the 2PA-induced PL amplitude, which is expected to be quadratic in case where 2PA is the dominant absorption mechanism, and the excitation intensity is not too high [64]. As can be seen, quadratic function can approximate the experimental data well (Figure 7.2). Two data points obtained at the highest powers were not included in the fit, because such high intensities started to create permanent damage to the sample.

Next, I extract an absolute value of the 2PA cross sections for b-polarized light at 840 nm by monitoring how the transmittivity of a sample changes when the incident intensity changes. This techniques can provide absolute 2PA cross sections only if the spatial and temporal profiles of the beam are known with good accuracy. Because
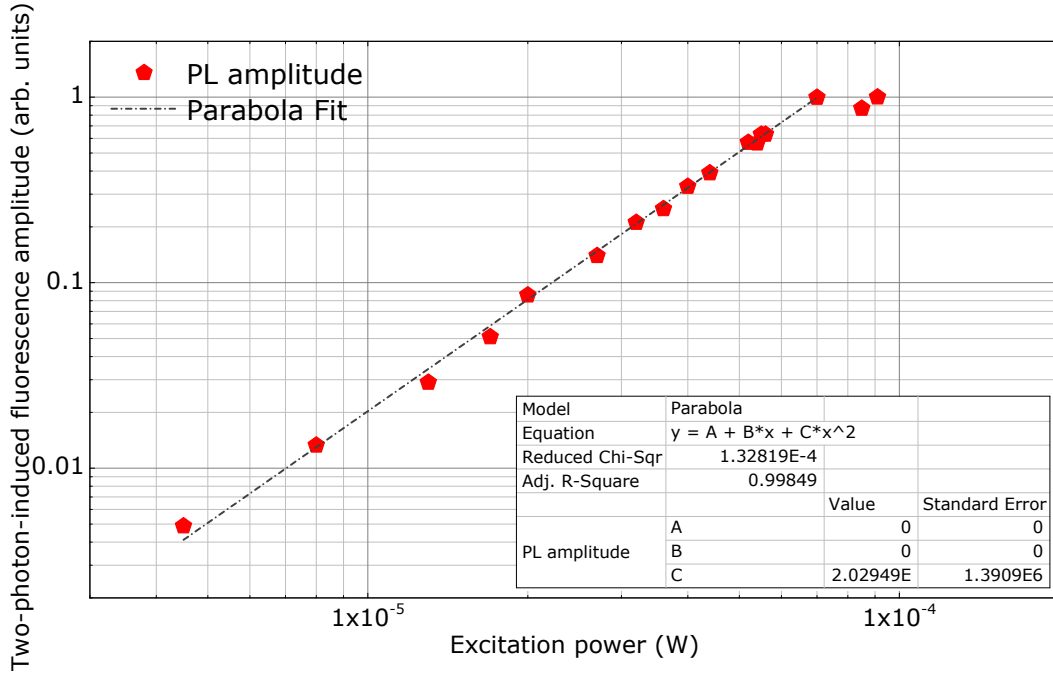
Figure 7.2: Log-log plot highlighting a quadratic dependence of the 2PA-induced fluorescence intensity on the excitation power.

ground state depletion [64] was not explicitly included in the equations I used to process the data, I performed this experiment in a small beam attenuation regime, as can be seen in Figure 7.3. Further, I calculated the nonlinear transmittivity using data from Figire 7.3, as shown in Figure 7.4. Figure 7.5 shows same tranmittivity data on a conventional lin-log plot.

Inset in Fig. 7.4 shows an expression I used to fit the experimental transmittivity data, which takes into account the spatial intensity distribution (nearly perfect Gaussian) in the beam (Figure 7.6). Here, β is the two-photon absorption coefficient, R is the reflection coefficient (calculated using Fresnel equations), L is the sample thickness, ω is the beam waist (Figure 7.6), and P_{max} is the peak laser pulse power. Quantities shown in red were measured independently and their values were directly
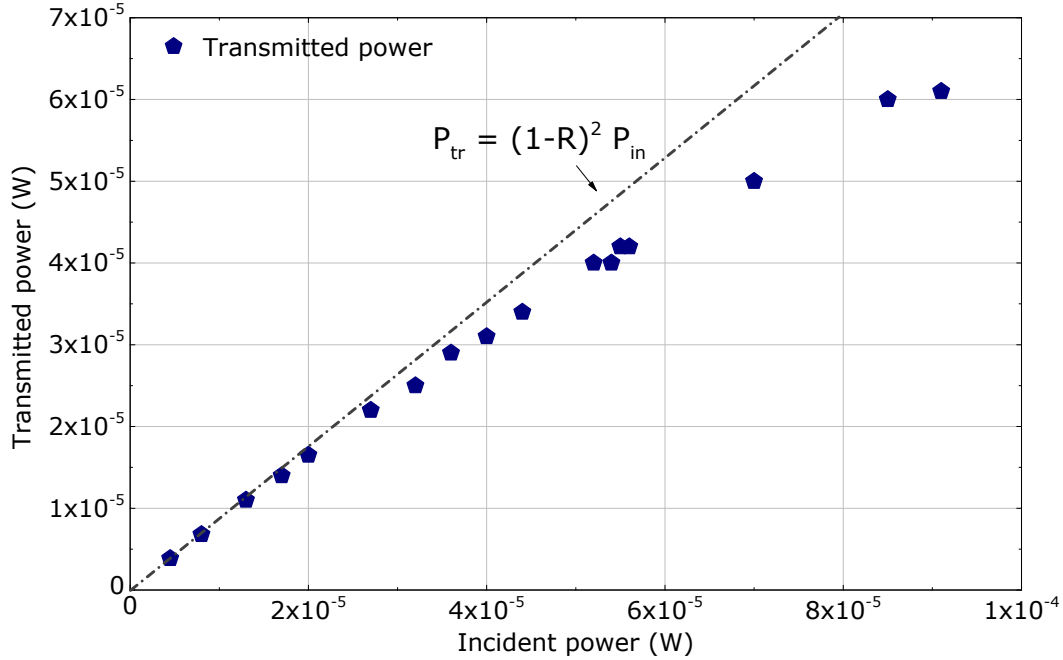
Figure 7.3: Dependence of the power of transmitted light through a rubrene crystal on the power of incident light. Dash-dotted line represents an expected transmitted power behavior in the absence of 2PA, where only reflection losses are responsible for beam attenuation.

used in this expression to fit the transmittivity data.

Fit yields the value of the two-photon absorption coefficient $\beta = (1.5\pm0.1)\times10^{-15}$ m/W, which corresponds to the two-photon absorption cross-section $\sigma = 2.53\times10^{-57}$ m^4 s $photon^{-1}$, or 25 GM, in good agreement with typical values measured in common dyes, which are of the order of 10 GM (1 GM $= 10^{-50}$ cm^4 s $photon^{-1}$, the large scaling factor was historically introduced in order that 2-photon absorption cross-sections of common dyes would have convenient values).

Further investigations are needed to obtain a full spectrum of two-photon absorption cross-section (including its anisotropy in the material), which will ultimately provide important new knowledge on the nature of the electronic states that can be
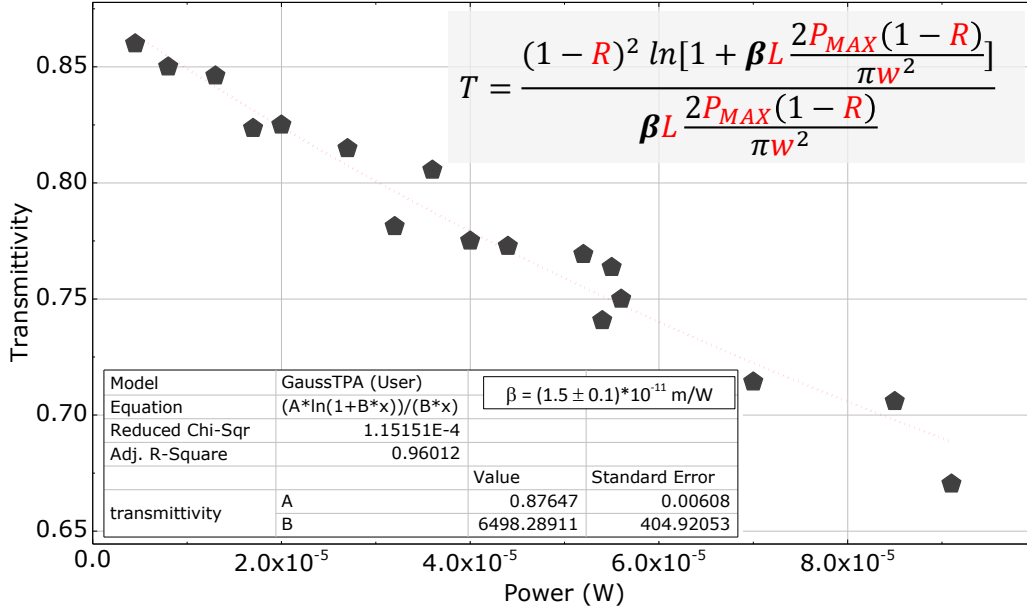
Figure 7.4: Nonlinear transmittivity of a rubrene single crystal as a function of incident light power. Inset: an expression used to fit the transmittivity data. Values in red were determined independently.

reached via two-photon absorption in rubrene molecular single crystals.

7.2 Conclusions and outlook

The organic molecular crystal is the system where the nano-scale details of inter-molecular charge transfer are reflected most accurately in macroscopic charge transport properties, and is the ideal playground for research on inter-molecular charge transfer, leading to information that can be valuable in general, important also for situations that do not directly involve single crystals. Fundamental investigations
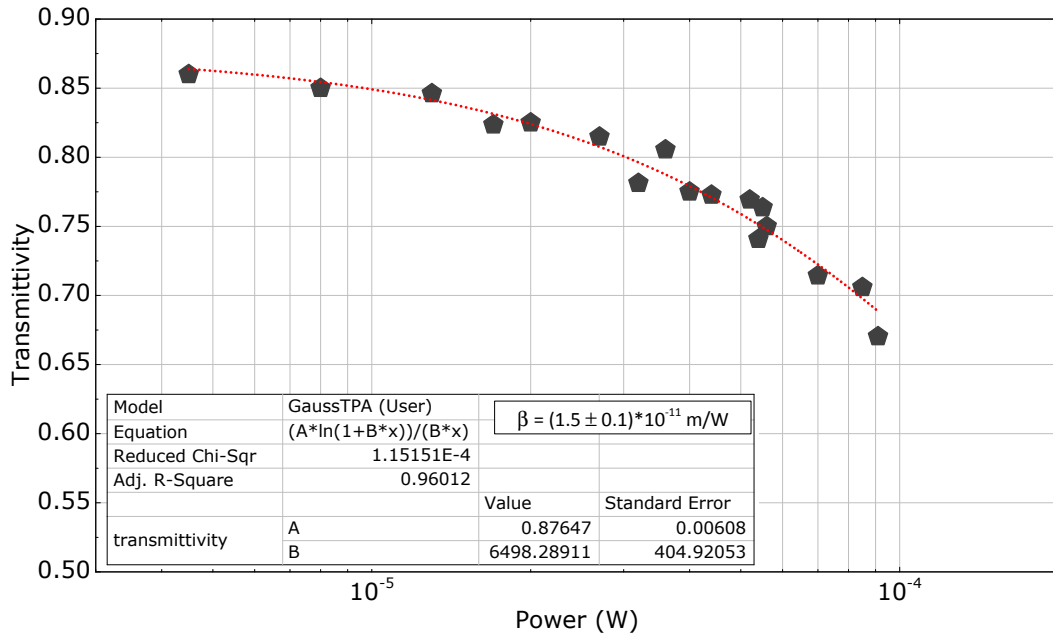
Figure 7.5: Lin-log plot of the nonlinear transmittivity of a rubrene single crystal versus incident laser beam power at 840 nm.

in the best organic molecular crystals available today should allow new insights into the transport mechanisms of a new system, similar to what happened when good quality semiconductors first became available.

Given the investigation of exciton diffusion described above, it would be interesting to connect the new results with the problem of exciton dissociation, and to more closely investigate the origin of the defects responsible for exciton dissociation into charge carriers, including the manner in which they interact with photoinduced molecular excitons.

Several laser based techniques that can be used to study the photoexcitation process itself were already demonstrated [13–15, 65], providing information about exciton creation to exciton dissociation, free-carrier lifetimes, and the related quantum
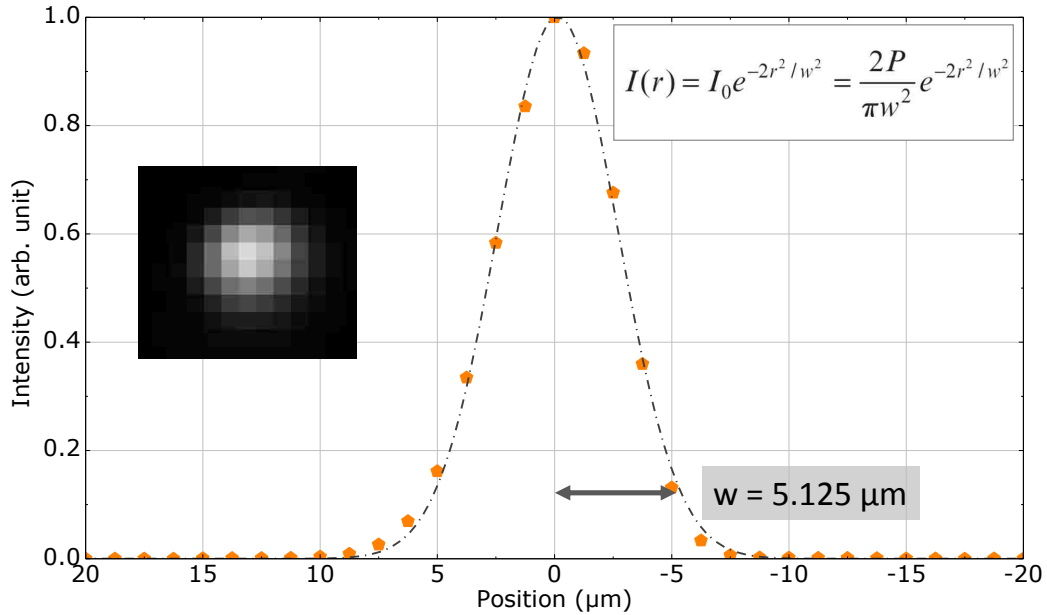
Figure 7.6: Spatial intensity distribution in the laser beam. Inset: image of the laser spot on the surface of a rubrene crystal obtained by a CCD camera (left); expression used to fit the intensity profile (right): r is the distance from the beam axis, ω is the beam waist, I_0 is the intensity on the beam axis, P is a total power in the laser beam.

efficiencies. Additional investigations that can clarify the evolution of the primary excitation into free carriers include "Pump and Probe" experiments with a tunable picosecond pulse for the initial excitation and a second tunable pulse to detect the evolution of the excitonic states. By identifying and recognizing the spectral signatures of different excited states and how the excitation moves from one to the other, this kind of investigation will allow to answer the question about the role played by charge-transfer excitons, triplet excitons, and the interaction with extrinsic defects

in rubrene.

Even though many "plastic electronics" systems that have been demonstrated are based on amorphous materials or polymers, ordered molecular systems provide an alternative way to gain insight into the physical processes responsible for transitions between neighboring molecules, and new fundamental knowledge acquired for single crystals will automatically be relevant also for disordered systems. Moreover, devices based on crystalline materials are a natural evolution from current designs based on amorphous films, and a better molecular order may be required in the future in order to increase the mobility and device performance, as an example for field effect transistors, or possibly even for the development of electrically pumped organic lasers. Thus, organic single crystals are likely to play a larger, important role as device technology progresses, and fundamental knowledge of transport in ordered assemblies is relevant even for nano-electronic systems based on only a few well-arranged organic molecules.

Bibliography

[1] Silinsh, E. & Capek, V. *Organic molecular crystals: interaction, localization, and transport phenomena* (American Institute of Physics, 1994). URL `http://books.google.com/books?id=Wh7wAAAAMAAJ`.

[2] Schwoerer, M. & Wolf, H. C. *Introduction*, 1–24 (Wiley-VCH Verlag GmbH, 2008). URL `http://dx.doi.org/10.1002/9783527618651.ch1`.

[3] Pope, M. & Swenberg, C. *Electronic processes in organic crystals and polymers*. Monographs on the physics and chemistry of materials (Oxford University Press, 1999). URL `http://books.google.com/books?id=AZVUAAAAMAAJ`.

[4] Sundar, V. C. *et al.* Elastomeric transistor stamps: Reversible probing of charge transport in organic crystals. *Science* **303**, 1644–1646 (2004). URL `http://www.sciencemag.org/content/303/5664/1644.abstract`.

[5] Briseno, A. *et al.* High-performance organic single-crystal transistors on flexible substrates. *Advanced Materials* **18**, 2320–2324 (2006). URL `http://dx.doi.org/10.1002/adma.200600634`.

[6] de Boer, R., Gershenson, M., Morpurgo, A. & Podzorov, V. Organic single-crystal field-effect transistors. *Phys. Status Solidi A* **201**, 1302 – 31 (2004). URL `http://dx.doi.org/10.1002/pssa.200404336`.

[7] Tseng, R., Chan, R., Tung, V. & Yang, Y. Anisotropy in organic single-crystal photovoltaic characteristics. *Adv. Mater.* **20**, 435–438 (2008). URL `http://dx.doi.org/10.1002/adma.200701374`.

[8] Shao, Y. & Yang, Y. White organic light-emitting diodes prepared by a fused organic solid solution method **86**, 073510 (2005). URL `http://dx.doi.org/10.1063/1.1866216`.

[9] Podzorov, V., Pudalov, V. & Gershenson, M. Field-effect transistors on rubrene single crystals with parylene gate insulator. *Appl. Phys. Lett.* **82**, 1739 – 41 (2003). URL `http://dx.doi.org/10.1063/1.1560869`.

[10] Podzorov, V. *et al.* Intrinsic charge transport on the surface of organic semi-conductors. *Phys. Rev. Lett.* **93**, 086602 (2004).

[11] Podzorov, V. & Gershenson, M. Photoinduced charge transfer across the interface between organic molecular crystals and polymers. *Phys. Rev. Lett.* **95**, 016602 – 1 (2005). URL `http://dx.doi.org/10.1103/PhysRevLett.95.016602`.

[12] Hasegawa, T. & Takeya, J. Organic field-effect transistors using single crystals. *Science and Technology of Advanced Materials* **10**, 024314 (2009). URL `http://stacks.iop.org/1468-6996/10/i=2/a=024314`.

[13] Najafov, H., Biaggio, I., Podzorov, V., Calhoun, M. F. & Gershenson, M. E. Primary photoexcitations and the origin of the photocurrent in rubrene single crystals. *Phys. Rev. Lett.* **96**, 056604 (2006). URL `http://link.aps.org/abstract/PRL/v96/e056604`.

[14] Najafov, H., Lyu, B., Biaggio, I. & Podzorov, V. Investigating the origin of the high photoconductivity of rubrene single crystals. *Phys. Rev. B* **77**, 125202 (2008).

[15] Najafov, H., Lyu, B., Biaggio, I. & Podzorov, V. Two mechanisms of exciton dissociation in rubrene single crystals. *Applied Physics Letters* **96**, 183302 (2010). URL `http://link.aip.org/link/?APL/96/183302/1`.

[16] Zeng, X. *et al.* Morphology and fluorescence spectra of rubrene single crystals grown by physical vapor transport. *Applied Surface Science* **253**, 6047 – 6051 (2007).

[17] Tavazzi, S. *et al.* Optical response and emission waveguiding in rubrene crystals. *Phys. Rev. B* **75**, 245416 (2007).

[18] Saeki, A., Seki, S., Takenobu, T., Iwasa, Y. & Tagawa, S. Mobility and dynamics of charge carriers in rubrene single crystals studied by flash-photolysis microwave conductivity and optical spectroscopy. *Adv. Mater.* **20**, 920–923 (2008). URL `http://dx.doi.org/10.1002/adma.200702463`.

[19] Stohr, R. J. *et al.* Enhanced photoluminescence from self-organized rubrene single crystal surface structures. *Applied Physics Letters* **96**, 231902 (2010). URL `http://link.aip.org/link/?APL/96/231902/1`.

[20] Müller, M., Langner, A., Krylova, O., Le Moal, E. & Sokolowski, M. Fluorescence spectroscopy of ultrathin molecular organic films on surfaces. *Applied Physics B: Lasers and Optics* **105**, 67–79 (2011). URL `http://dx.doi.org/10.1007/s00340-011-4764-0`. 10.1007/s00340-011-4764-0.

[21] Mitrofanov, O. *et al.* Role of synthesis for oxygen defect incorporation in crystalline rubrene. *Applied Physics Letters* **91**, 212106 (2007). URL `http://link.aip.org/link/?APL/91/212106/1`.

[22] Liu, H. *et al.* Up-conversion luminescence of crystalline rubrene without any sensitizers. *Organic Electronics* **11**, 946 – 950 (2010).

[23] Kloc, C., Tan, K. J., Toh, M. L., Zhang, K. K. & Xu, Y. P. Purity of rubrene single crystals. *Appl. Phys. A.* **95**, 219 (2009).

[24] Huang, L. *et al.* Rubrene micro-crystals from solution routes: their crystallography, morphology and optical properties. *J. Mater. Chem.* **20**, 159–166 (2010). URL `http://dx.doi.org/10.1039/B914334C`.

[25] Ma, L. *et al.* Singlet fission in rubrene single crystal: direct observation by femtosecond pump-probe spectroscopy. *Phys. Chem. Chem. Phys.* – (2012). URL `http://dx.doi.org/10.1039/C2CP40449D`.

[26] Kaminsky, W. *WinXMorph*: a computer program to draw crystal morphology, growth sectors and cross sections with export files in VRML V2.0 utf8-virtual reality format. *Journal of Applied Crystallography* **38**, 566–567 (2005). URL `http://dx.doi.org/10.1107/S0021889805012148`.

[27] Jurchescu, O. D., Meetsma, A. & Palstra, T. T. M. Low-temperature structure of rubrene single crystals grown by vapor transport. *Acta Crystallographica Section B* **B62**, 330ñ334 (2006).

[28] Käfer, D., Ruppel, L., Witte, G. & Wöll, C. Role of molecular conformations in rubrene thin film growth. *Phys. Rev. Lett.* **95**, 166602 (2005). URL `http://link.aps.org/doi/10.1103/PhysRevLett.95.166602`.

[29] Petrenko, T., Krylova, O., Neese, F. & Sokolowski, M. Optical absorption and emission properties of rubrene: insight from a combined experimental and theoretical study. *New Journal of Physics* **11**, 015001 (2009). URL `http://stacks.iop.org/1367-2630/11/i=1/a=015001`.

[30] Laudise, R., Kloc, C., Simpkins, P. & Siegrist, T. Physical vapor growth of organic semiconductors. *Journal of Crystal Growth* **187**, 449 – 454 (1998). URL `http://www.sciencedirect.com/science/article/pii/S0022024898000347`.

[31] El Helou, M., Medenbach, O. & Witte, G. Rubrene microcrystals: A route to investigate surface morphology and bulk anisotropies of organic semiconductors. *Crystal Growth and Design* **10**, 3496–3501 (2010). URL `http://pubs.acs.org/doi/abs/10.1021/cg1003758`.

[32] Sai, N., Tiago, M. L., Chelikowsky, J. R. & Reboredo, F. A. Optical spectra and exchange-correlation effects in molecular crystals. *Phys. Rev. B* **77**, 161306 (2008).

[33] Tavazzi, S. *et al.* Generalized ellipsometry and dielectric tensor of rubrene single crystals. *Journal of Applied Physics* **102**, 023107 (2007). URL `http://link.aip.org/link/?JAP/102/023107/1`.

[34] Irkhin, P. & Biaggio, I. Direct imaging of anisotropic exciton diffusion and triplet diffusion length in rubrene single crystals. *Phys. Rev. Lett.* **107**, 017402 (2011).

[35] Köstler, S. *et al.* Direct condensation method for the preparation of organic-nanoparticle dispersions. *Advanced Materials* **21**, 2505–2510 (2009). URL `http://dx.doi.org/10.1002/adma.200900081`.

[36] Park, D. H. *et al.* Highly bright and sharp light emission of a single nanoparticle of crystalline rubrene. *J. Mater. Chem.* **21**, 8002–8007 (2011). URL `http://dx.doi.org/10.1039/C1JM10530B`.

[37] Lee, J. W. *et al.* Light-emitting rubrene nanowire arrays: A comparison with rubrene single crystals. *Advanced Functional Materials* **19**, 704–710 (2009). URL `http://dx.doi.org/10.1002/adfm.200801180`.

[38] Mitrofanov, O. *et al.* Oxygen-related band gap state in single crystal rubrene. *Phys. Rev. Lett.* **97**, 166601 (2006). URL `http://link.aps.org/abstract/PRL/v97/e166601`.

[39] Chen, Y., Lee, B., Fu, D. & Podzorov, V. The origin of a 650 nm photoluminescence band in rubrene. *Advanced Materials* (2011). URL `http://dx.doi.org/10.1002/adma.201102294`.

[40] Fumagalli, E. *et al.* Oxidation dynamics of epitaxial rubrene ultrathin films. *Chemistry of Materials* **23**, 3246–3253 (2011). URL `http://pubs.acs.org/doi/abs/10.1021/cm201230j`. `http://pubs.acs.org/doi/pdf/10.1021/cm201230j`.

[41] Krellner, C. *et al.* Density of bulk trap states in organic semiconductor crystals: Discrete levels induced by oxygen in rubrene. *Physical Review B (Condensed Matter and Materials Physics)* **75**, 245115 (2007). URL `http://link.aps.org/abstract/PRB/v75/e245115`.

[42] Nakayama, Y. *et al.* Direct observation of the electronic states of single crystalline rubrene under ambient condition by photoelectron yield spectroscopy. *Applied Physics Letters* **93**, 173305 (2008). URL `http://link.aip.org/link/?APL/93/173305/1`.

[43] Song, X. *et al.* Role of oxygen incorporation in electronic properties of rubrene films. *Applied Physics Letters* **97**, 032106 (2010). URL `http://link.aip.org/link/?APL/97/032106/1`.

[44] Weinberg-Wolf, J. R., McNeil, L. E., Liu, S. & Kloc, C. Evidence of low intermolecular coupling in rubrene single crystals by raman scattering. *Journal of Physics: Condensed Matter* **19**, 276204 (2007). URL `http://stacks.iop.org/0953-8984/19/i=27/a=276204`.

[45] Ridley, J. & Zerner, M. An intermediate neglect of differential overlap technique for spectroscopy: Pyrrole and the azines. *Theoretical Chemistry Accounts: Theory, Computation, and Modeling (Theoretica Chimica*

Acta) **32**, 111–134 (1973). URL `http://dx.doi.org/10.1007/BF00528484`. 10.1007/BF00528484.

[46] Zerner, M. C., Loew, G. H., Kirchner, R. F. & Mueller-Westerhoff, U. T. An intermediate neglect of differential overlap technique for spectroscopy of transition-metal complexes. ferrocene. *Journal of the American Chemical Society* **102**, 589–599 (1980). URL `http://pubs.acs.org/doi/abs/10.1021/ja00522a025`. `http://pubs.acs.org/doi/pdf/10.1021/ja00522a025`.

[47] Frisch, M. J. *et al.* Gaussian 03 Revision C.02. Gaussian Inc. Wallingford CT 2004.

[48] Bates, D. & Estermann, I. *Advances in Atomic and Molecular Physics*. Serial Publication Series (Academic Press, 1980). URL `http://books.google.com/books?id=-WoXq_sHtSwC`.

[49] Yu, G., Gao, J., Hummelen, J. C., Wudl, F. & Heeger, A. J. Polymer photovoltaic cells: Enhanced efficiencies via a network of internal donor-acceptor heterojunctions. *Science* **270**, 1789–1791 (1995). URL `http://www.sciencemag.org/content/270/5243/1789.abstract`.

[50] Peumans, P., Uchida, S. & Forrest, S. R. Efficient bulk heterojunction photovoltaic cells using small-molecular-weight organic thin films. *Nature* **425**, 158–162 (2003). URL `http://dx.doi.org/10.1038/nature01949`.

[51] Avakian, P. & Merrifield, R. E. Experimental determination of the diffusion length of triplet excitons in anthracene crystals. *Phys. Rev. Lett.* **13**, 541–543 (1964).

[52] Ern, V., Avakian, P. & Merrifield, R. E. Diffusion of triplet excitons in anthracene crystals. *Phys. Rev.* **148**, 862–867 (1966).

[53] Williams, D. F. & Adolph, J. Diffusion length of triplet excitons in anthracene crystals. *The Journal of Chemical Physics* **46**, 4252–4254 (1967). URL http://link.aip.org/link/?JCP/46/4252/1.

[54] Vaubel, G. & Kallmann, H. Diffusion length and lifetime of triplet excitons and crystal absorption coefficient in tetracene determined from photocurrent measurements. *phys. stat. sol. (b)* **35**, 789–792 (1969). URL http://dx.doi.org/10.1002/pssb.19690350228.

[55] Arden, W., Kotant, M. & Peter, L. M. Triplet exciton decay processes in crystalline tetracene. *phys. stat. sol. (b)* **75**, 621–631 (1976). URL http://dx.doi.org/10.1002/pssb.2220750226.

[56] Terao, Y., Sasabe, H. & Adachi, C. Correlation of hole mobility, exciton diffusion length, and solar cell characteristics in phthalocyanine/fullerene organic solar cells. *Applied Physics Letters* **90**, 103515 (2007). URL http://link.aip.org/link/?APL/90/103515/1.

[57] Gommans, H., Schols, S., Kadashchuk, A., Heremans, P. & Meskers, S. C. J. Exciton diffusion length and lifetime in subphthalocyanine films.

The Journal of Physical Chemistry C **113**, 2974–2979 (2009). URL
http://pubs.acs.org/doi/abs/10.1021/jp809802q.

[58] Aladekomo, J. B., Arnold, S. & Pope, M. Triplet exciton diffusion and double
photon absorption in tetracene. *physica status solidi (b)* **80**, 333–340 (1977).
URL http://dx.doi.org/10.1002/pssb.2220800139.

[59] Najafov, H., Lee, B., Zhou, Q., Feldman, L. C. & Podzorov, V. Observation
of long-range exciton diffusion in highly ordered organic semiconductors. *Nat.
Mater.* **9**, 938–943 (2010). URL http://dx.doi.org/10.1038/nmat2872.

[60] Sanvitto, D. *et al.* Observation of charge transport by nega-
tively charged excitons. *Science* **294**, 837–839 (2001). URL
http://www.sciencemag.org/content/294/5543/837.abstract.

[61] Ryasnyanskiy, A. & Biaggio, I. Triplet exciton dynamics in
rubrene single crystals. *Phys. Rev. B* **84**, 193203 (2011). URL
http://link.aps.org/doi/10.1103/PhysRevB.84.193203.

[62] Tarasov, V. V., Zoriniants, G. E., Shushin, A. I. & Triebel, M. M. The role
of spin-lattice relaxation in magnetic field effects on the luminescence of amor-
phous and polycrystalline rubrene films. *Chemical Physics Letters* **267**, 58 –
64 (1997).

[63] Da Silva Filho, D. A., Kim, E.-G. & Bredas, J.-L. Transport prop-
erties in the rubrene crystal: Electronic coupling and vibrational reor-
ganization energy. *Advanced Materials* **17**, 1072 – 1076 (2005). URL
http://dx.doi.org/10.1002/adma.200401866.

[64] Rumi, M. & Perry, J. W. Two-photon absorption: an overview of measurements and principles. *Adv. Opt. Photon.* **2**, 451–518 (2010). URL `http://aop.osa.org/abstract.cfm?URI=aop-2-4-451`.

[65] Najafov, H., Biaggio, I., Chuang, T.-K. & Hatalis, M. K. Exciton dissociation by a static electric field followed by nanoscale charge transport in ppv polymer films. *Phys. Rev. B* **73**, 125202 (2006).

Publications

Articles in peer-reviewed journals

1. "Direct Imaging of Anisotropic Exciton Diffusion and Triplet Diffusion Length in Rubrene Single Crystals." P. Irkhin and I. Biaggio, *Phys. Rev. Lett.*, **2011**, 107, 017402

2. "Absorption and Photoluminescence Spectroscopy of Rubrene Single Crystals." P. Irkhin, A. Ryasnyanskiy, M. Koehler, and I. Biaggio, *accepted to Phys. Rev. B*

3. "Two-Photon Spectroscopy of Rubrene Single Crystals." P. Irkhin, A. Ryasnyanskiy, C. F. N. Marchiori, D. J. Gulin, M. Koehler, and I. Biaggio, *in preparation*

4. "Fission and Fusion of Excitons in Rubrene Single Crystals" P. Irkhin, I. Biaggio, *in preparation*

5. "Effect of Proton Irradiation on Exciton Diffusion Length in Rubrene Single Crystals." P. Irkhin, I. Biaggio, T. Zimmerling, B. Batlogg, *in preparation*

Conference contributions

1. "Direct Imaging of Large Exciton Diffusion in the Organic Molecular Crystal Rubrene." P. Irkhin and I. Biaggio, *MRS Fall Meeting, 2011*

2. "Two-Photon Spectroscopy of Rubrene Single Crystals." P. Irkhin, A. Ryasnyanskiy, and I. Biaggio, *MRS Fall Meeting, 2011*

3. "Photoluminescence Spectroscopy of Rubrene Single Crystals." P. Irkhin, A. Ryasnyanskiy, and I. Biaggio, *MRS Fall Meeting, 2011*

4. "Direct Imaging of Anisotropic Exciton Diffusion in Rubrene Organic Molecular Single Crystals." P. Irkhin and I. Biaggio, *COT Open House, 2011*

5. "One- and Two-photon Excited State Spectroscopy of Rubrene Single Crystals'.' P. Irkhin, M. Koehler, I. Biaggio, *MRS Fall Meeting, 2012*

6. "Theoretical Interpretation of the Intrinsic Photoluminescence Properties of Rubrene Single Crystals." C. F. N. Marchiori, M. Koehler, P. Irkhin, A. Ryasnyanskiy, I. Biaggio, *Brazilian MRS Meeting, 2012*

Vita

Pavel Irkhin was born on March 25th, 1985 in Znamensk, Russia. He performed his undergraduate studies in Moscow Engineering Physics Institute between 2002 and 2006, then started his graduate studies at Lehigh University in Fall 2007, where he was awarded a Master's degree in Physics in January of 2010, and his PhD in Physics in September of 2012.